

# **Ice Cloud Properties in Ice-Over-Water Cloud Systems**

## **Using TRMM VIRS and TMI Data**

Patrick Minnis<sup>1</sup>, Jianping Huang<sup>2</sup>, Bing Lin<sup>1</sup>, Yuhong Yi<sup>2</sup>, Robert F. Arduini<sup>3</sup>,  
Tai-Fang Fan<sup>3</sup>, J. Kirk Ayers<sup>2</sup>, and Gerald G. Mace<sup>4</sup>

<sup>1</sup>NASA Langley Research Center, Hampton, VA. 23681

<sup>2</sup>College of Atmospheric Sciences, Lanzhou University, Lanzhou, China

<sup>3</sup>Analytical Services & Materials, Inc., Hampton, VA 23666

<sup>4</sup>SAIC, Hampton, VA 23666

<sup>5</sup>University of Utah, Salt Lake City, UT

Submitted to the *Journal of Geophysical Research*

June 2006

## **Abstract**

A multi-layered cloud retrieval system (MCRS) is updated and used to estimate ice water path in maritime ice-over-water clouds using Visible and Infrared Scanner (VIRS) and TRMM Microwave Imager (TMI) measurements from the Tropical Rainfall Measuring Mission spacecraft between January and August 1998. Lookup tables of top-of-atmosphere 0.65- $\mu\text{m}$  reflectance are developed for ice-over-water cloud systems using radiative transfer calculations with various combinations of ice-over-water cloud layers. The liquid and ice water paths, LWP and IWP, respectively, are determined with the MCRS using these lookup tables with a combination of microwave (MW), visible (VIS), and infrared (IR) data. LWP, determined directly from the TMI MW data, is used to define the lower-level cloud properties to select the proper lookup table. The properties of the upper-level ice clouds, such as optical depth and effective size, are then derived using the Visible Infrared Solar-infrared Split-window Technique (VISST), which matches the VIRS IR, 3.9- $\mu\text{m}$ , and VIS data to the multilayer-cloud lookup table reflectances and a set of emittance parameterizations. Initial comparisons with surface-based radar retrievals suggest that this enhanced MCRS can significantly improve the accuracy and decrease the IWP in overlapped clouds by 42% and 13% compared to using the single-layer VISST and an earlier simplified MW-VIS-IR (MVI) differencing method, respectively, for ice-over-water cloud systems. The tropical distribution of ice-over-water clouds is the same as derived earlier from combined TMI and VIRS data, but the new values of IWP and optical depth are slightly larger than the older MVI values, and exceed those of single-layered layered clouds by 7% and 11%, respectively. The mean IWP from the MCRS is 8-14% greater than that retrieved from radar retrievals of overlapped clouds over two surface sites and the standard deviations of

the differences are similar to those for single-layered clouds. Examples of a method for applying the MCRS over land without microwave data yield similar differences with the surface retrievals. By combining the MCRS with other techniques that focus primarily on optically thin cirrus over low water clouds, it will be possible to more fully assess the IWP in all conditions over ocean except for precipitating systems.

INDEX TERMS: 0320 Cloud physics and chemistry; 0321 Cloud/radiation interaction; 3360 Remote sensing; 0365 Troposphere: composition and chemistry.

## 1. Introduction

Satellite retrievals of ice cloud properties, essential for characterizing the global atmospheric hydrological and radiation budgets, are often complicated by the occurrence of multi-layered overlapped clouds. Most current satellite cloud retrievals are based on the assumption that all clouds are comprised of a homogeneous single layer within the field-of-view of the satellite measurements, despite the frequent occurrence of overlapped cloud systems. Cloud overlap can introduce large errors in the retrieval of many cloud properties such as ice water path (*IWP*), cloud height, optical depth, thermodynamic phase, and effective particle size [e.g., *Huang et al.*, 2005]. For multi-layered systems with ice clouds overlying water clouds, the influence of liquid water clouds on satellite-observed radiances observed is one of the greatest impediments to accurately determining cloud ice amount. The optical depth derived from the reflected visible radiance represents the combined effects of all cloud layers. When the reflected radiance is interpreted using a single-layer (SL) ice cloud model, the ice-cloud optical depth can be significantly overestimated because the underlying water cloud generally increases the reflectance. It is clear that the underlying clouds must be properly characterized for a more accurate retrieval of cloud properties in overlapped systems.

To retrieve the properties of overlapped cloud systems, it is first necessary to identify which pixels in satellite imagery contain multilayered clouds. Several techniques for discriminating single-layer from multi-layered clouds have been developed and applied to data taken over broad areas of the globe. Over water surfaces, the combined use of microwave (MW), visible (VIS), and infrared (IR) data can be used to detect liquid water underneath higher clouds as long as the layers are separated by effective radiating temperatures of 8 K or more. *Lin and Rossow* [1996] and *Lin*



*et al.* [1998] applied this MW-VIS-IR (MVI) method to poorly matched data sets from different satellite platforms, while *Ho et al.* [2003] applied it to well-matched Visible Infrared Scanner (VIRS) and Tropical Rainfall Measuring Mission (TRMM) Microwave Imager (TMI) data on the TRMM satellite. *Pavlonis and Heidinger* [2004] developed an 11-12  $\mu\text{m}$  brightness temperature difference (BTD) method combined with VIS imager data to detect thin cirrus clouds over water clouds and analyzed a large global dataset that only excludes bright surfaces such as snow and deserts [*Heidinger and Pavlonis*, 2005]. *Chang and Li* [2005a] combined a CO<sub>2</sub>-slicing infrared method and VIS-IR data (COVIR) to detect a similar variety of overlapped thin cirrus above liquid water clouds over the same range of surface types and analyzed global data over 4 months spanning a single year [*Chang and Li*, 2005b].

Once a pixel containing overlapped pixels is identified, the cloud properties in each layer need to be estimated. *Chang and Li* [2005a] take advantage of the effective emissivity of the CO<sub>2</sub>-slicing method to assign an initial value to the ice cloud optical depth, then, the VIS-IR radiances are used together with a two-layer cloud reflectance model, an IR emissivity parameterization, and contextual information to iterate to a solution for the upper and lower cloud properties. For the overlapped (OL) clouds detected by the MVI approach, the liquid water path (*LWP*) is estimated directly from the MW data providing the anchor for estimating *IWP*. The simplest approach to analyze the MVI-detected clouds, designated the MVI retrieval technique, retrieves the total cloud water path (*TWP*) using a VIS-IR technique that assumes that the entire cloud consists of ice particles. The *IWP* is estimated as the difference between the *TWP* and MW-derived *LWP* [*Lin and Rossow*, 1996; *Lin et al.*, 1998; *Ho et al.*, 2003]. Recognizing that the radiative fields emanating from combined ice and water cloud layers are generally not equivalent

to those with the same *TWP*, *Huang et al.* [2005] developed a more rigorous multilayer cloud retrieval system (MCRS) that explicitly treats both the low-level cloud as part of the background radiation field for the upper layer cloud and the ice-cloud contribution to the TOA radiance to estimate the *IWP* values. In the initial version of the MCRS, *Huang et al.* [2005] used a parameterization of the adding-doubling (AD) radiative transfer method by combining the low-layer cloud with the surface to produce a background radiance for the retrieval of the ice cloud properties. It significantly improved the accuracy of the retrieved *IWP* but is subject to greater uncertainty than more exact calculations of radiative transfer [*Arduini et al.*, 2002].

To reduce that uncertainty and produce a more accurate assessment of OL tropical maritime clouds, this study first upgrades the MCRS and then applies it to VIRS and TMI data. The improved MCRS uses lookup tables of reflectance based on radiative transfer calculations of combined ice and water cloud reflectance. The background in the radiative transfer model can be either a land or ocean surface. This enhanced version is more accurate and is applicable to a broader range of boundary conditions. The cloud properties and VIRS radiances from the latest edition of the VIRS retrievals by the Clouds and the Earth's Radiant Energy System (CERES, see *Wielicki et al.* [1998]) project are matched with TMI data and then reanalyzed with the MCRS. A preliminary validation of the results is performed using data from surface observations. The information derived using the MCRS should improve our understanding of the distribution of ice water path and provide a reference for evaluating the *IWP* generated by climate models over the tropical oceans.

## 2. Data

The data used here consist of MW, VIS, and IR measurements taken by the *TRMM* satellite over open oceans equatorward of 38° latitude. *TRMM* is in a 350-km circular orbit with a 35°-inclination angle [Kummerow *et al.* 1998]. *TRMM* data are analyzed here only for 1 January through 31 August 1998, the period when the CERES scanner was operational. The *TRMM* TMI is a nine-channel, passive MW radiometer measuring radiances at frequencies of 10.65, 19.35, 21.3, 37.0 and 85.5 GHz. All channels have both vertically (V) and horizontally (H) polarized measurements except for the 21.3-GHz channel, which has only vertical polarization. TMI scans conically with an incident angle of 52.8° at the sea surface and yields a swath width of ~758.5 km. The 85.5- and 37-GHz effective footprints are 7 km (down-track direction) by 5 km (cross-track direction) and 16 km by 9 km, respectively. The plane-parallel MW radiation transfer model of Lin *et al.* [1998a] was used to simulate  $T_b$  for all TMI channels. A lookup table was built for various atmospheric conditions including a range of cloud temperatures ( $T_w$ ),  $LWP$ , atmospheric column water vapor ( $WV$ ), near-surface wind speed ( $WS$ ), and sea surface temperature ( $SST$ ). For each cloudy pixel,  $LWP$  and  $T_w$  can be retrieved from the lookup table simultaneously using  $SST$ ,  $WS$ ,  $WV$ , and  $T_{b_{37H}}$  and  $T_{b_{85V}}$  measurements as in Ho *et al.* [2003], hereafter denoted as HO3.

The *TRMM* VIRS is a five-channel imager that measures radiances at 0.65 (VIS), 1.64, 3.75 (SIR), 10.8 (IR), and 12.0  $\mu\text{m}$  with a nominal 2-km spatial resolution. The VIRS cross-track scan yields coverage roughly between 38°N and 38°S. The VIRS radiance data were used to retrieve cloud fraction, thermodynamic phase (water or ice phase), optical depth, effective particle size, and water path (WP) as well as surface skin temperature, cloud-top temperature  $T_c$ ,

and cloud-top height  $z$  for the CERES project [Minnis *et al.* 1995, 2002]. Ice and liquid water path retrievals were calculated for each cloudy VIRS pixel using the cloud optical depth and effective particle size estimated VIS-IR-SIR-Split-window Technique (VISST) assuming a single cloud phase and layer for all clouds in the atmospheric column [Minnis *et al.* 1995, 1998]. This study uses the same datasets and retrievals as HO3 except that the CERES *TRMM* Edition-2 VIRS cloud properties and spectral radiances [Minnis *et al.* 2002] are used here instead of the Edition-1 cloud properties [Minnis *et al.* 1999]. In addition to other changes, the Edition-2 algorithm uses a different visible reflectance parameterization [Arduini *et al.*, 2002] and accounts for absorption of visible wavelength radiation by water vapor. Relative to the Edition-1 retrievals, these two changes tend to reduce the optical depth for thin clouds, increase the optical depth for thicker clouds, and reduce the solar zenith angle (SZA) dependence of the optical depth retrievals.

Since TMI has much larger footprints ( $\sim 20$  km) than VIRS, the VIRS cloud products were convolved with TMI measurements to produce equivalent VIRS cloud retrievals within the TMI footprints. Only the TMI pixels containing more than 15% cloudiness from the convolved VIRS-TMI data are used here. The resulting dataset constitutes 81.6% of all TMI pixels taken over the oceans. Because TMI and VIRS are on the same spacecraft, the temporal and spatial mismatches of VIRS and TMI measurements are negligible. The detailed collocation and retrieval processes for the *TRMM* data can be found in HO3.

### 3. Methodologies

#### 3.1 Two-Layer Model and Retrieval Algorithm

A cloud AD radiation transfer model [Minnis *et al.* 1993] is used to characterize the reflectance fields for multilayered clouds. The upper and lower layers consist of ice particles and water droplets, respectively. Figure 1 shows the schematic diagram of scattering and absorption processes for this simple two-layer cloud AD model. The 0.65- $\mu\text{m}$  reflectance,  $R_v$ , at particular solar zenith ( $\theta_0$ ), viewing zenith ( $\theta$ ), and relative azimuth ( $\psi$ ) angles (Table 1) were computed with the AD model using 11 ice cloud models and 7 water cloud models [Minnis *et al.* 1998] for ice cloud optical depths,  $\tau_i$ , ranging from 0 to 128 and water cloud optical,  $\tau_w$ , ranging from 0 to 32. Three scattering layers,  $i = 1, 3$ , with reflectances,  $\rho_{Ri}$ , and Rayleigh optical depths,  $\tau_{Ri}$ , are separated by the two cloud layers and sandwiched between an ozone absorption layer and a surface with reflectance,  $\rho_s$ . The incoming radiation is indicated in Figure 1 as the spectral solar constant,  $F_o$ , multiplied by  $\mu_o = \cos\theta_o$ . The computed values of  $R_v$  were compiled in type-specific lookup tables. For the lookup tables, the high cloud was placed at 200 hPa and the water cloud was located at 900 hPa. The ozone absorption is computed in the highest layer of the model using an optical depth,  $\tau_{AI}$  of 0.0332. Changing the upper and lower cloud pressures by 200 hPa resulted in reflectance differences of less than 1%. The largest reflectance differences occur for  $\tau_i < 4$  for  $\tau_w < 1$ , a case that is unlikely to be discerned with the MCRS. The error range for the remaining combinations was generally smaller than  $\pm 0.5\%$ . Thus, there is only minimal impact using fixed cloud pressures for the retrievals.

The reflectances for any set of angles, optical depths, and lower-cloud  $r_e$  are estimated from the lookup tables using nearest-node values and interpolations with combinations of linear and Lagrangian methods as in *Minnis et al.* [1998]. Given the  $LWP$  and  $r_e$  of the lower-layer water cloud, a set of TOA VIS reflectances can be easily computed using these lookup tables of reflectance for each optical depth node and ice particle size.

Examples of reflectances from combined cloud layers are given in Figures 2 and 3. Figure 2 shows  $\rho$  at  $\theta_0 = 45^\circ$  as a function of viewing and illumination angles from the AD calculations using a fixed upper-layer ice cloud optical depth ( $\tau_1 = 8$ ) and effective particle diameter ( $De = 67 \mu\text{m}$ ), that yields  $IWP = 160 \text{ gm}^{-2}$ , over water clouds with four different  $LWP$ 's.  $R_v$  increases and becomes more isotropic as  $LWP$  rises from 0 to  $150 \text{ gm}^{-2}$ . The anisotropy is different, however, from that expected for a pure ice cloud with the same albedo. The anisotropic difference and reflectance increase cause the VISST retrievals to overestimate  $IWP$  and  $TWP$  when a lower cloud is present, due to the one-layer assumption. Figure 3 shows  $R_v$  for the same conditions except that the  $TWP$  is fixed at  $200 \text{ gm}^{-2}$  and  $LWP$  and  $IWP$  are varied as indicated in the plots. Figures 2a and 3a are similar in pattern because both have no water influence. However, Figures 2c and 3d are also quite similar despite the former having a value of  $TWP$  that is  $60 \text{ gm}^{-2}$  greater than that in the latter plot. These plots illustrate the importance of properly treating the reflectance field in multilayered conditions. For example, in Figure 2c at  $\theta = 60^\circ$  and  $\psi=45^\circ$ ,  $R_v = 0.74$ . A SL ice cloud with the same  $TWP$  would produce  $R_v = 0.65$ . A retrieval based on  $R_v$  for the cloud system in Figure 2c using the assumption that the entire cloud is ice phase would yield  $IWP = TWP = 345 \text{ gm}^{-2}$ . In this case, the retrieved  $IWP$  and  $TWP$  are overestimated by  $245 \text{ gm}^{-2}$  and  $145 \text{ gm}^{-2}$ , respectively.

Figure 4 shows the variation of TOA diffuse albedo  $A_v$  as a function of  $\tau_l$  and  $\tau_w$ . The diffuse albedo is significantly impacted by lower-layer water clouds and is especially sensitive to their optical depth  $\tau_w$ . For a given value of  $A_v$ ,  $\tau_l$  for an overlapped cloud ( $\tau_w > 0$ ) should be smaller than  $\tau_l$  for a SL ice cloud. For example, if  $A_v = 0.6$ , the case with  $\tau_w = 0$  yields  $\tau_l \approx 12$ , but if  $\tau_w = 10$ ,  $\tau_l \approx 5$ . Very similar results are found with the other ice models (not shown here). It is clear that as  $\tau_w$  increases, the sensitivity to changes in  $\tau_l$  decreases so that estimates of when  $\tau_l < 2$  are more uncertain than those for thicker high clouds. The values of  $A_v$  for different ice cloud models at  $\tau_w = 2$  and  $r_e = 12 \mu\text{m}$  in Figure 5 vary by as much as 0.10 ( $\tau_l = 10$ ) for differing ice cloud particle diameters. For a given albedo,  $\tau_l$  varies by as much as 35% depending on the value of  $D_e$ . The sensitivity of TOA diffuse albedos to varying  $r_e$  at  $\tau_w = 30$  and  $D_e = 30.36 \mu\text{m}$  is shown in Figure 6. For a range of  $r_e$  between 2 and 32  $\mu\text{m}$ ,  $A_v$  varies by 0.10 for  $\tau_l = 0.25$  and by 0.06 for  $\tau_l = 10$ , approaching zero at larger values of  $\tau_l$ . If only values of  $r_e$  between 8 and 32  $\mu\text{m}$  are considered, however, the  $A_v$  range is only 0.02 or less. Since the average value of  $r_e$  is typically between 9 and 18  $\mu\text{m}$  over ocean areas (e.g., Minnis *et al.* [2002]), the variations in  $r_e$  should not have a significant impact on the derived *IWP* for most cases. Similar results are expected for the bidirectional reflectances because the angular reflectance patterns of SL low clouds vary minimally for a given optical depth as seen in Figure 5 of Minnis *et al.* [1998].

To improve the accuracy of ice cloud property retrievals, a global multi-layered cloud retrieval system (MCRS) is developed. Initially, the SL VISST retrieval is used to detect cloudy pixels and estimate the cloud properties by treating each cloudy pixel as a *single-layered* cloud.

Next, the combined MW, visible and IR (MVI) method [Lin *et al.* 1998a,b] is used to detect OL cloudy pixels. The MVI technique detects overlapping clouds by using the difference between cloud water temperature ( $T_w$ ) retrieved from TMI microwave data and the cloud effective temperature ( $T_e$ ) derived from VISST [Lin *et al.* 1998b]. The third step is to estimate the optical depth of the lower-layer water cloud. The optical depth of the lower-layer water cloud can be written as

$$\tau_w = 0.75 Q_{vis}(r_e) LWP / r_e. \quad (1)$$

$$r_e = r_0 + r_l * LWP, \quad (2)$$

where  $Q_{vis}(r_e)$  is the extinction efficiency for a given effective droplet radius. For the ocean,  $r_0 = 12$ ,  $r_l = 0.0186$ . These values of  $r_e$  and  $\tau_w$ , derived from the statistics of SL water clouds based on 8 months of CERES VIRS-based retrievals, were used to select the proper lookup tables. TOA radiances are then computed for every combination of the specified low-level cloud and the upper-layer ice cloud. In formulation, the MCRS retrieval follows the iterative VISST procedure resulting in recalculation of the effective ice crystal diameter ( $De$ ),  $\tau_l$ , and  $IWP$  for the upper-layer cloud. In practice, the value of  $De$  found from the initial VISST retrieval is assumed to be valid for the upper-layer cloud. Therefore, the MCRS only needs to match the two-layer cloud LUT reflectances to the observed reflectances for the given viewing and illumination angles,  $\tau_w$ , and  $De$ . In all cases, the surface albedo is set to 0.04, a value close to the diffuse surface albedo at 0.64



$\mu\text{m}$ . Since relatively thick two-layer cloud systems are being analyzed here, the diffuse albedo approximation should apply for the overlapped cases. The VISST used for the SL cases employs a variable surface reflectance field.

### 3.2 *Overlapped Cloud Detection*

The value of  $T_w$  retrieved from TMI data represents the mean cloud water temperature of the integrated cloud column whereas  $T_c$  derived from the VIRS data represents the temperature near the top of the cloud for optically thick clouds [Minnis *et al.* 1993]. Therefore, when the difference,  $\Delta T_{wc} = T_w - T_c$ , is significantly positive, it is highly likely that the observed system consists of OL clouds [Lin *et al.* 1998b] or, at a minimum, of an ice cloud contiguous with an underlying water cloud. In this study, two special overcast groups are selected and studied. The conditions for selecting the two groups are

(1) single-layer high ice clouds (ICLD): 100% ice phase,  $LWP \leq 40 \text{ gm}^{-2}$ ,  $T_w > 290 \text{ K}$ ,

$T_c < 273 \text{ K}$ ,  $|T_s - T_w| < 5 \text{ K}$  and  $T_s - T_c > 36 \text{ K}$ , where  $T_s = SST$ .

(2) overlapped cloud (OCLD): 100% ice phase,  $T_w < 290 \text{ K}$ ,  $T_c < 273 \text{ K}$ ,

$T_w - T_c > 15 \text{ K}$ ,  $T_s - T_c > 36 \text{ K}$ , and  $LWP > 0 \text{ gm}^{-2}$ .

The thermodynamic (ice/water) phase of the highest cloud was determined by the CERES VIRS analysis [Minnis *et al.* 2002]. The thresholds used here exclude a significant portion of the overcast cloud data including mixed and liquid water phase clouds as well as ice clouds that are classified as precipitating so that  $LWP$  cannot be retrieved using the MW technique.

## 4. Results

Only ice-over-water clouds are the focus of this study. The COLD and ICLD groups together constitute about 13.5% of all overcast cases and half of all VIRS pixels classified as ice phase using the initial VISST analysis. The remainder of the ice phase clouds are either in the precipitating or fractionally cloudy categories. The average ice cloud coverage for the entire domain is 19.3%.

### 4.1. Overlapped cloud amounts

Figure 7 shows scatter plots of  $T_w$  with  $T_c$  for each of the two groups for tropical ocean ( $20^\circ\text{S} - 20^\circ\text{N}$ ) regions during July 1998. The relationships between  $T_w$  and  $T_c$  are distinct for each group. For SL ice clouds in Figure 7a,  $T_w$  is very narrowly distributed around 300 K. In contrast,  $T_c$  is very low, ranging from 210 to 265 K with a mean of 239.4 K and standard deviation of 12.1 K. In the ICLD case, there is almost no liquid cloud water in the atmosphere ( $LWP \sim \text{zero}$ ), and the TMI radiances are directly from the sea surface with some attenuation by atmospheric water vapor and other trace gases. Thus, the estimated  $T_w$  values are not really cloud water temperatures; instead, they are more representative of the  $SST$ . The negative linear correlation coefficient ( $R = -0.22$ ) between  $T_w$  and  $T_c$  further demonstrates a relationship between  $T_w$  and  $SST$ . Fewer SL cirrus clouds occur over the colder waters of the Tropics where low-level clouds and subsidence predominate.

The OL cloud systems (OCLD) have a strong positive correlation between  $T_w$  and  $T_c$  (Figure 7b). The mean  $T_w$  (260.5K) is about 27.5 K greater than the average  $T_c$  values (233.0 K), although the standard deviations, 11.3 K and 12.5 K, respectively, are similar. In addition to the

presence of OL clouds, this large difference arises from the fact that the MW radiation emanates from much lower cloud layers than the IR radiances measured by VIRS. This result confirms that significant differences between  $T_w$  and  $T_c$  can be used as the critical condition for identifying cloud overlap.

The frequency distributions of OL clouds for July 1998 over the domain ocean areas are shown in Figure 8 as functions of two parameters derived from the TMI. The frequency of occurrence (FOC) is defined as the percentage of OL clouds in a given parameter bin relative to the total number of OCLD pixels. More than 70% of the lower-layer clouds (Figure 8a) are relatively thin water clouds with  $LWP < 100 \text{ gm}^{-2}$ ;  $LWP$  peaks at 30 and 70  $\text{gm}^{-2}$ . OCLD's occur most often when  $SST = 289.5 \text{ K}$  (Figure 8b), while a secondary peak is seen at 302 K. More than 55% of OCLD pixels are found in regions with  $SST < 295 \text{ K}$ .

Figure 9 shows the FOC variations of three OCLD types for different zonal bands from January through August 1998. The occurrence frequency is defined as the percentage of the overlap type relative to the total number of OCLD pixels. These three types are (1) ice-over-warm-water cloud systems (IOWW), where  $T_w > 273 \text{ K}$ ; (2) ice-over-supercooled water cloud systems (IOSW), where  $255 \text{ K} < T_w < 273 \text{ K}$ ; and (3) ice-over-extremely-supercooled water clouds (IOEW) with  $T_w < 255 \text{ K}$ . For IOSW and IOEW, the lower-layer clouds may consist of a mixture of both ice and water particles while both thin cirrus and thick anvils can comprise the upper-layer clouds. The deepest convective clouds are likely to be confined to the IOEW category. The IOSW clouds (dotted curves) are the major type of ice-over-water cloud systems in all regions, accounting for more than 55% of all OCLD pixels compared to 15% and 30% for IOEW (dashed) and IOWW (solid), respectively. These results are consistent with ship

observations [*Hahn et al.* 1982], which show that in the Tropics, cirrus clouds overlap altostratus, cumulus and cumulonimbus more often than they occur over stratus and stratocumulus.

Globally between 37°N and 37°S, the FOCs of the three OCLD types vary minimally with season (Figure 9a). IOEW increases by ~8% from January to August while IOSW decreases by a similar amount. The most striking seasonal changes occur between 20°N and 37°N (Figure 9b), where IOSW drops by 20% as IOEW doubles from 25% from winter to summer. IOWW peaks in April and falls to a minimum during summer. Presumably, the seasonal rise in IOEW is linked to increased deep convection during summer. Deep convection should raise liquid water up to greater altitudes underneath anvil-produced cirrus than that generated by baroclinic disturbances, which are more common in other seasons and produce many layers of water clouds beneath the cirrus shields. A similar convergence of the IOSW and IOEW occurs in the Tropics (Figure 9c) during the boreal summer when the ITCZ is most developed. The seasonal variability in the three OCLD types is least in the southern subtropics where IOEW and IOWW are of the same magnitude.

## ***4.2 Cloud properties***

The cloud properties from each category and analysis type were averaged for each month and season and plotted only for the area between 30°S and 30°N to minimize the impact of sampling noise that occurs at the higher latitudes. Figure 10 shows the mean values of *De* during June-August (JJA) 1998 for the ICLD VISST retrievals and the OCLD MCRS retrievals. Since the iteration to recalculate *De* was not used here in the MCRS, the values for OCLD are same for

both the VISST and the MCRS analyses, so the former is not shown. These results indicate that  $De$  for the OCLD cases is similar to but slightly larger than the ICLD values. Similar results were found for the other two seasons, January-February (JF) and March-May (MAM), as seen in Table 2. The mean values of  $De$  for all seasons combined are 61.6 and 58.6  $\mu\text{m}$  for the ICLD and OCLD cases, respectively.

VISST optical depths for all ice clouds during JJA generally range from 0.5 to 32 with a few scattered regions with  $\tau_I > 32$  (Figure 11a). If only the OCLD cases are considered (Figure 11b), the bottom end of the range is increased up to 2 or 3, while many new regions have means exceeding 32. The very thickest clouds are probably excluded from the OCLD category because of precipitation, while the thinnest clouds are unlikely to be OL. The mean value of  $\tau_I$  in Figure 11b is 19.2. Most of the overcast ice clouds without significant liquid water beneath them (ICLD, Figure 11c) have  $\tau_I < 16$  with some extremely low mean values ( $\tau_I < 0.5$ ) off the coast of Brazil. The largest values are seen off the coasts of southern Asia and eastern Australia and in the Gulf of Mexico. Overall,  $\tau_I = 9.6$ . Application of the MCRS to the OCLD cases (Figure 11d) substantially reduces the number of regions with  $\tau_I > 16$  and raises the number of areas with  $\tau_I < 8$  resulting in an average optical depth of 11.3. This represents a 59% reduction in  $\tau_I$  for the OCLD cases. Instead of being twice as thick as their SL counterparts, the MCRS reveals that the OL ice clouds detected here are only 11% thicker, on average, than the ICLDs. These results are typical for all seasons as indicated in Table 2.

Combining  $\tau_I$  and  $De$  yields  $IWP$ , which is plotted for the various algorithms in Figures 12 and 13 for JF and JJA, respectively. For all of the ice clouds retrieved with the VISST (Figures

12a and 13a), the monthly means range from less than  $4 \text{ gm}^{-2}$  in the subsidence zones to over  $1024 \text{ gm}^{-2}$  in a few areas. The range in the means for the OCLD subsets (Figures 12b and 13b) of the total VISST retrievals is narrowed with the minimum between  $64$  and  $128 \text{ gm}^{-2}$  during both seasons. The ICLD optical depths (Figures 12c and 13c) vary over the same range as the total VISST retrievals. The largest values occur over the Caribbean during winter and in the southern Indian Ocean during boreal summer. The MCRS decreases IWP for the OCLD cases (Figures 12d and 13d) to values that are more like the ICLD values than the VISST OCLD results. The maximum values, found mainly in the Intertropical Convergence Zone (ITCZ) in both figures, do not exceed  $1024 \text{ gm}^{-2}$ . The differences between the VISST and MCRS OCLD cases, shown in Figures 12e and 13e, are all positive and mostly greater than  $200 \text{ gm}^{-2}$  in the ITCZ. Seasonally, the mean VISST OCLD IWP ranges from  $355 \text{ gm}^{-2}$  in winter to  $393 \text{ gm}^{-2}$  in summer (Table 2) with a mean of  $370 \text{ gm}^{-2}$ ,  $157 \text{ gm}^{-2}$  greater than the MCRS IWP. The MCRS OCLD IWP also peaks in summer, while the mean ICLD IWP remains relatively over the 8-month period. The former is less than 7% greater than ICLD IWP, on average, and 42% greater than its VISST counterpart.

## 5. Discussion

### 5.1 Validation

Validation of this retrieval method is difficult because reliable independent estimates of IWP in OL clouds are limited to retrievals using cloud radar data or in situ data. The latter are quite rare and do not provide robust statistics, thus the radar option is the most feasible approach. Earlier studies of SL ice clouds showed that the VISST yields quite reasonable

estimates of IWP compared to radar-based retrievals [e.g., *Mace et al.* 2005]. Most cloud radar data are taken over land where the satellite-borne MW radiometer yields unreliable measurements of LWP. However, uplooking surface-based MW data can substitute for the TMI measurements. Preliminary validation of the MCRS IWP is accomplished by comparison with simultaneous retrievals from the Millimeter Cloud Radar (MMCR) radar at the Atmospheric Radiation Program (ARM) Southern Great Plains Central Facility (SCF) in Oklahoma. The 10 cases of ice-over-water clouds for 3 days in 2000 used by *Huang et al.* [2005] are also employed here for comparison. These cases cover a wide range of viewing, illumination, and scattering angles. Figure 14 compares the *IWP* derived from the Eighth Geostationary Operational Environmental Satellite (GOES-8), which substitutes for VIRS, and surface-based MW data using the MCRS, from GOES-8 using VISST [*Minnis et al.* 2004], and from the MMCR using the algorithm of *Mace et al.* [2002]. For the MCRS retrieval, *LWP* is estimated from the ARM MW radiometer measurements as in *Lin et al.* [2001]. As expected, the MCRS consistently produces smaller values of *IWP* than VISST. In all of the cases, the MCRS *IWP* is close to that from the MMCR retrieval. The differences are greatest for case 7 when the MCRS *IWP* is approximately  $218 \text{ gm}^{-2}$  less than the VISST retrieval. For these cases, the mean difference between the MCRS and MMCR *IWPs* is  $9 \text{ gm}^{-2}$ , which is 13.8% of the mean MMCR value of  $65 \text{ gm}^{-2}$  (Table 3). This bias is a factor of 3 smaller than the parameterization-based MCRS [*Huang et al.* 2005] demonstrating the increase accuracy expected from using explicit multilayered cloud model calculations. The standard deviation of the differences is  $30 \text{ gm}^{-2}$ . The mean difference is almost 3.5 times smaller than the mean VISST-MMCR difference. *Huang et al.* [2006] found a similar difference (8%) when comparing satellite-based MCRS retrievals with MMCR retrievals taken

from tropical Manus Island. Although the validation results are limited, it is clear that the MCRS represents a marked improvement over the SL VISST retrieval. The MCRS reduces the  $TWP$ , on average, due to the lower value of  $IWP$ . Analysis of additional matched satellite data and ground observations are required to fully validate the MCRS. Nevertheless, the initial results indicate the MCRS yields  $IWP$  values that are as accurate as SL VISST retrievals [e.g., *Mace et al.* 2005].

Figure 14 includes an additional set of data points labeled as MCRS-Sounding Data or MCRS-SD. These represent results based on the MCRS using GOES-8 data and  $LWP_{SD}$ , which is estimated from ARM SCF rawinsonde soundings using

$$LWP_{SD} = \int_{Z_B}^{Z_T} \eta(RH, T) * LWC(Z) dZ \quad (3)$$

where  $Z_B$ ,  $Z_T$ , are the cloud base and top heights, respectively, and  $\eta(RH, T)$  is the cloud probability function that is determined from relative humidity  $RH$  and temperature  $T$  [*Minnis et al.* 2005].  $LWC$  is the adiabatic liquid water content. This algorithm, defined as the *MCRS-SD*, yields values of  $IWP$  that are as close to the MMCR results as the standard MCRS, which uses the MW radiometer retrievals of  $LWP$ . The mean MCRS-SD  $IWP$  ( $60 \text{ gm}^{-2}$ ) is smaller than both the MCRS and MMCR values. These results suggest that reliable soundings could be used as substitutes for MW radiometer data in the MCRS over land surfaces.

## 5.2 Dependencies

Figure 15 shows a comparison of ice-cloud optical depths derived from VISST and MCRS as a function of  $LWP$  for the July 1998 results. For the VISST retrievals,  $\tau_i$  increases almost linearly with rising  $LWP$ . This is expected because thin water clouds will not cause a large



VISST retrieval error, which is also consistent with the AD calculations (c.f., Figures 2 and 3). The rise in  $R_v$  with increasing  $LWP$  causes the VISST to overestimate  $\tau_1$ . The effects of the lower layer cloud, however, are nearly removed by MCRS and there is only a slight downward trend in the MCRS-retrieved  $\tau_1$  associated with increasing  $LWP$  for  $LWP > 110 \text{ gm}^{-2}$ . The mean  $\tau_1$  drops to 7.7 from 13.9, which is very close to the mean value for SL ice clouds (7.8) for the same number of samples within the domain. The variations of  $\tau_1$  from VISST and MCRS as functions of  $T_w$ , are shown in Figure 16. MCRS retrieves significantly lower values of  $\tau_1$  than VISST for all  $T_w$  bins. The ice-cloud optical depth decreases with increasing  $T_w$  for both the VISST and MCRS optical depths. This result suggests that the ice clouds are generally thicker in ice-over cool water clouds than in ice-over warm water clouds.

The dependence of  $\tau_1$  on SZA for both MCRS and VISST is plotted in Figure 17. The values of  $\tau_1$  are relatively flat for  $\text{SZA} < 65^\circ$ , but increase for larger SZAs. This variation may be due to a greater occurrence of anvil and deep convective clouds during early morning and late afternoon hours than other times over tropics. However, it may also be the result of model errors since three-dimensional effects, not included in the retrieval models, are more pronounced at the higher SZAs. Additional research is necessary to determine how much of the effect is algorithmic and how much is due to actual changes in cloud thickness near the terminator times.

Figure 18 compares the mean  $IWP$  derived from VISST, MVI and MCRS as a function of  $LWP$ . The  $IWP$  derived from VISST represents the combined effects of all cloud layers, thus,  $IWP = TWP$ . In that case,  $IWP$  increases substantially with increasing  $LWP$  just as  $\tau_1$  did in Figure 15. The  $IWP$  derived from both MVI and MCRS have the same behavior, a small downward

trend with increasing  $LWP$  for  $LWP > 110 \text{ gm}^{-2}$ . In all cases, mean  $IWP$  from MVI is 10 -50  $\text{gm}^{-2}$  larger than that derived by the MCRS.

Histograms of  $IWP$  derived from VISST, MVI, and MCRS for ice-over-water clouds and the  $IWP$  derived from VISST for SL ice clouds are shown in Figure 19. As expected, the mean  $IWP$  values derived from the MCRS in July 1998 (Figure 19b) are considerably less than those derived from VISST. The mean  $IWP$  decreases from 283 to 173  $\text{mg}^{-2}$ , a value only 10% larger than the SL ice cloud (ICLD) mean value of 157  $\text{gm}^{-2}$ . The multilayered cloud pixels with  $IWP < 100 \text{ gm}^{-2}$  comprise more than 50% of the data for MCRS retrievals compared to only 18% for VISST retrievals. For the lowest category ( $IWP < 100 \text{ gm}^{-2}$ ), the MCRS frequency is only 6% less than the ICLD frequency. The MVI and ICLD frequency distributions are also similar but differ more in all bins compared to MCRS and ICLD. The first bin includes negative values of  $IWP$  derived using the MVI indicating that the MVI-MCRS  $IWP$  difference of less than 20  $\text{gm}^{-2}$ , would be much larger if negative  $IWP$  retrievals were not included. Similar results are also found in all other analyzed months as seen for January 1998 (Figure 19a). In this case, the mean  $IWP$  from MCRS is 5% less than the ICLD mean. The agreement in each bin is even closer than seen in Figure 19b. Overall, the consistency in the MCRS OCLD and the VISST ICLD frequency distributions for all bins further demonstrates the improvements provided by the MCRS.

### 5.3 Comparisons with other data

The occurrence frequencies and geographical distributions of OCLD in this analysis are nearly same as those reported by HO3 and are not shown here. For discussing comparisons with other analyses, the reader is referred to the distribution of OCLD occurrence from Figures 9 and

10 of HO3. *Heidinger and Pavlonis* [2005] found that their patterns of OL clouds were similar to those of HO3, but they found slightly more OL cloud cover. The patterns of overlapped high cloud cover in *Chang and Li* [2005b] for analyses of 2001 *Terra* Moderate Resolution Imaging Spectroradiometer (MODIS) data are quite similar to those of HO3 for July, but different for January over the Pacific and north Atlantic Oceans. A strong El Niño, underway during January 1998 and ended before July 1998, may explain the differences in the patterns seen in January. While difficult to determine precisely from disparate figures, the OLCD frequency of occurrence from HO3 in the Tropics appears to be slightly greater than that in *Chang and Li* [2005b]. More OL cloudiness is expected when using higher resolution data like MODIS because the OCLD definition requires 100% ice cloud cover in the 20-km TMI footprint. That definition excludes the edges of large clouds and scattered cirrus over lower clouds. The apparent discrepancies between the comparisons of HO3 with the results of *Heidinger and Pavlonis* [2005] and *Chang and Li* [2005b] may be due to algorithmic differences. The latter may be more constrained in terms of  $\tau_L$ .

HO3 applied the MVI technique to the 1998 CERES Edition-1 VIRS data and found that the IWP for the OCLD data was 6-10% less than that for the ICLD TMI pixels. The MCRS applied to the Edition-2 data for the same period yields OCLD IWP means that are 10% larger than the ICLD values indicating some significant changes. *Chang and Li* [2005b] found that  $\tau_L$  in the COVIR OL cloud cases ranged between 0 and 5 with an annual mean of 1.54 over ocean areas. This value is much smaller than the results in Table 2 and is clearly due to the limitations of applying the COVIR technique to optically thin high clouds. The MCRS detects and retrieves ice-over-water clouds regardless of  $\tau_L$ , except when the clouds are precipitating. Nevertheless, the

ratios of  $\tau_1$  for OL clouds to that for SL clouds are similar for the two methods: 11% for the MCRS and 8% for *Chang and Li* [2005b] when the latter is based on the same classes of high clouds. A value of  $\tau_1 = 5$  corresponds to  $94 \text{ gm}^{-2}$  for  $De = 61 \text{ }\mu\text{m}$ . Thus, the COVIR results correspond to roughly 53% of the MCRS OCLD results (i.e,  $IWP < 100 \text{ gm}^{-2}$ ) in Figure 19. The difference in frequency of occurrence discussed earlier is most likely considerably less than 50% so the OCLD cases do not account for all of the thin cirrus over water cloud cases. Thus, while there is commonality between OCLD and the *Chang and Li* [2005b] results, neither accounts for all OL clouds, even over ocean. Together, the two techniques should account for the impact of LWP in most ice-over-water clouds, but conditions where they provide overlapping results need to be defined. Neither technique can unscramble the relative contributions of LWP and IWP in precipitating clouds.

## 6. Concluding Remarks

A more rigorous multilayered cloud retrieval system has been developed to improve the determination of high cloud properties in multilayered cloud systems over water surfaces. The MCRS attempts a more realistic interpretation of the radiance field than earlier methods because explicit radiative transfer calculations were used to simulate the observed radiances for two-layer cloud systems. Initial comparisons with independent data show that the MCRS produces a more accurate retrieval of ice water path than the simple differencing techniques (e.g., MVI) used in the past. The MCRS method is quite appropriate for interpreting the radiances when the high cloud

has a relatively large optical depth ( $\tau_1 > 2$ ). For thinner ice clouds, a more accurate retrieval might be possible using other methods. This issue needs further exploration.

The results show that, compared to ice cloud properties derived using a SL cloud model, the MCRS reduces both the ice cloud optical depth and IWP by 42%, on average. Because the technique is more realistic and the preliminary validation data indicate good agreement with cloud radar retrievals, these new results should be considered more accurate than previous estimates of overlapped ice and water clouds in the Tropics. Hence, they should be immediately valuable for assessing certain aspects of climate models. However, it is obvious that they only represent a portion of the overlapped cloud conditions.

Despite the great strides made during the last few years in untangling the characteristics of overlapped cloud systems, many challenges remain in the effort to monitor the cloud water budget, especially for multilayered clouds. The current viable multilayer retrieval methods are applicable only during daytime and only in certain conditions. The COVIR approach can be used over most surfaces but is limited to optically thin clouds, while the MCRS is confined to ocean surfaces and cannot be used for precipitating clouds. Application of the MCRS over land would require either accurate knowledge of microwave surface emissivities, which can be highly variable in time, or numerical weather analyses that provide reliable estimates of water vapor profiles in the lower troposphere. The latter could be used in the MCRS-SD, as demonstrated in this study. For satellites lacking CO<sub>2</sub>-slicing channels, the BTD method could be used to detect multilayered clouds and a multi-spectral infrared technique could be used to retrieve the upper and lower-layer cloud properties as in *Minnis et al.* [2005]. Assuming such techniques could be implemented, the problems of performing the retrievals at night and for precipitating clouds still remain. Perhaps,

with the aid of the recently launched cloud radar on *CloudSat* [Stephens *et al.* 2002] and the lidar on the CALIPSO [Winker *et al.* 2002] satellites, current techniques can be further validated and improved and new methods can be developed for retrieving multi-layered cloud properties at night from passive satellite imagery. As the current results demonstrate, however, the MCRS can serve as an important component of any future comprehensive cloud monitoring system.

## **ACKNOWLEDGEMENTS**

This research was supported by the NASA Science Mission through the Clouds and the Earth's Radiant Energy System Project, the NASA Aviation Safety Program through the NASA Advanced Satellite Aviation-weather Products Initiative, and the Office of Biological and Environmental Research of U.S. Department of Energy through the Interagency Agreements DE-AI02-97ER62341 and DE-AI02-02ER63319 as part of the Atmospheric Radiation Measurement program. The CERES data were obtained from the NASA Langley Research Center Atmospheric Sciences Data Center. Special thanks to Yan Chen for her assistance in preparing the graphics.

## References

- Arduini, R. F., P. Minnis, and D. F. Young (2002), Investigation of a visible reflectance parameterization for determining cloud properties in multilayered clouds, *Proc. 11<sup>th</sup> AMS Conf. Cloud Physics*, Ogden, UT, June 3-7, CD-ROM, P2.4.
- Chang, F.-L. and Z. Li (2005a), A new method for detection of cirrus overlapping water clouds and determination of their optical properties, *J. Atmos. Sci.*, **62**, 3993-4009.
- Chang, F.-L. and Z. Li (2005b), A near-global climatology of single-layer and overlapped clouds and their optical properties from Terra/MODIS data using a new algorithm, *J. Climate*, **18**, 4752-4771.
- Heidinger, A. K. and M. J. Pavlonis (2005), Global daytime distribution of overlapping cirrus cloud from NOAA's Advanced Very High Resolution Radiometer, *J. Climate*, **18**, 4772-4784.
- Ho, S.-P., B. Lin, P. Minnis, and T.-F. Fan (2003), Estimation of cloud vertical structure and water amount over tropical oceans using VIRS and TMI data, *J. Geophys. Res.*, **108**, 10.1029/2002JD003298.
- Huang, J., P. Minnis, B. Lin, Y. Yi, M. M. Khaiyer, R. F. Arduini, and G. G. Mace (2005), Advanced retrievals of multilayered cloud properties using multi-sensor and multi-spectral measurements, *J. Geophys. Res.*, **110**, 10.1029/2004JD005101.
- Huang, J., P. Minnis, B. Lin, Y. Yi, T.-F. Fan, S. Sun-Mack, and J. K. Ayers (2006), Determination of ice water path in ice-over-water cloud systems using combined MODIS and AMSR-E measurements, Submitted to *Geophys. Res. Lett.*
- Lin, B., and W. B. Rossow (1996), Seasonal variation of liquid and ice water path in non-precipitating clouds over oceans, *J. Climate*, **9**, 2890-2902.

- Lin, B., B. Wielicki, P. Minnis, and W. B. Rossow (1998a), Estimation of water cloud properties from satellite microwave, infrared and visible measurements in oceanic environments, I: Microwave brightness temperature simulations, *J. Geophys. Res.*, *103*, 3873-3886.
- Lin, B., P. Minnis, B. Wielicki, D. R. Doelling, R. Palikonda, D. F. Young, and T. Uttal (1998b), Estimation of water cloud properties from satellite microwave, infrared and visible measurements in oceanic environments, II: Results, *J. Geophys. Res.*, *103*, 3887-3905.
- Lin, B., P. Minnis, A. Fan, J. A. Curry, and H. Gerber (2001), Comparison of cloud liquid water paths derived from in situ and microwave radiometer data taken during the SHEBA/FIREACE, *Geophys. Res. Lett.*, *28*, 975-978.
- Kummerow, C., W. Barnes, T. Kozu, J. Shiue, and J. Simpson (1998), The Tropical Rainfall Measuring Mission (TRMM) sensor package, *J. Atmos. Ocean. Technol.*, *15*, 809-817.
- Mace, G. G., A. J. Heymsfield, and M. R. Poellot (2002), On retrieving the microphysical properties of cirrus clouds using the moments of the millimeter-wavelength Doppler spectrum, *J. Geophys. Res.*, *107*, 4815-4841.
- Mace, G. G., Y. Zhang, S. Platnick, M. D. King, P. Minnis, and P. Yang (2005), Evaluation of cirrus cloud properties from MODIS radiances using cloud properties derived from ground-based data collected at the ARM SGP site, *J. Appl. Meteorol.*, *44*, 221-240.
- Minnis, P., Y. Takano, and K.-N. Liou (1993), Inference of cirrus cloud properties using satellite-observed visible and infrared radiances, Part I: Parameterization of radiance fields, *J. Atmos. Sci.*, *50*, 1279-1304.
- Minnis, P., D. P. Kratz, J. A. Coakley, Jr., M. D. King, D. P. Garber, P. W. Heck, S. Mayor, D. F. Young, and R. F. Arduini (1995), Cloud Optical Property Retrieval (Subsystem 4.3),



"Clouds and the Earth's Radiant Energy System (CERES) Algorithm Theoretical Basis Document, Volume III: Cloud Optical Property Retrieval (Subsystem 4.3)", *NASA RP 1376 Vol. III*, edited by CERES Science Team, pp. 135-176.

Minnis, P., L. Nguyen, W. L. Smith, Jr., M. M. Khaiyer, R. Palikonda, D. A. Spangenberg, D. R. Doelling, D. Phan, G. D. Nowicki, P. W. Heck, and C. Wolff (2004), Real-time cloud, radiation, and aircraft icing parameters from GOES over the USA, *Proc. 13<sup>th</sup> AMS Conf. Satellite Oceanogr. and Meteorol.*, Norfolk, VA, Sept. 20-24, CD-ROM, P7.1.

Minnis, P., D. P. Garber, D. F. Young, R. F. Arduini, and Y. Takano (1998), Parameterization of reflectance and effective emittance for satellite remote sensing of cloud properties, *J. Atmos. Sci.*, *55*, 3313-3339.

Minnis, P., S. Sun-Mack, Y. Chen, H. Yi, J. Huang, L. Nguyen, and M. M. Khaiyer (2005), Detection and retrieval of multi-layered cloud properties using satellite data, *Proc. SPIE Europe Intl. Symp. Remote Sens., Remote Sens. Clouds and Atmos. X, Bruges, Belgium*, September 19-22, 5979, 597909, 9 pp.

Minnis, P., Y. Yi, J. Huang, and J. K. Ayers (2005), Relationships between radiosonde and RUC-2 meteorological conditions and cloud occurrence determined from ARM data, *J. Geophys. Res.*, *110*, doi:10.1029/2005JD006005.

Minnis, P., D. F. Young, B. A. Wielicki, P. W. Heck, X. Dong, L. L. Stowe, R. Welch (1999), CERES cloud properties derived from multispectral VIRS data, *Proc. The EOS/SPIE Symposium on Remote Sensing, Vol. 3867*, Florence, Italy, September 20-24, 91-102.

Minnis, P., D. F. Young, B. A. Wielicki, D. P. Kratz, P. W. Heck, S. Sun-Mack, Q. Z. Trepte, Y. Chen, S. L. Gibson, R. R. Brown (2002), Seasonal and diurnal variations of cloud properties

derived for CERES from VIRS and MODIS data, *Proc. 11<sup>th</sup> AMS Conf. Atmos. Rad.*, Ogden, UT, June 3-7, 20-23.

Pavlonis, M. J. and A. K. Heidinger, Daytime cloud overlap detection using AVHRR and VIIRS. *J. Appl. Meteorol.*, 43, 762-778, 2004.

Stephens, G. L., D. G. Vane, R. J. Boain, G. G. Mace, K. Sassen, Z. Wang, A. J. Illingworth, E. J. O'Connor, W. B. Rossow, S. L. Durden, S. D. Miller, R. T. Austing, A. Benedetti, C. Mitrescu (2002), The CloudSat mission and the A-Train, *Bull. Amer. Meteor. Soc.*, 83, 1771-1790.

Wielicki, B. A., B. R. Barkstrom, B. A., Baum, T. P. Charlock, R. N. Green, D. P. Kratz, R. B. Lee, P. Minnis, G. L. Smith, D. F. Young, R. D. Cess, J. A. Coakley, D. A. H. Crommelynck, L. Donner, R. Kandel, M. D. King, A. J. Miller, V. Ramanathan, D. A. Randall, L. L. Stowe, and R. M. Welch (1998), Clouds and the Earth's Radiant Energy System (CERES): Algorithm Overview, *IEEE Trans. Geosci. and Rem. Sens.*, 36, 1127-1141.

Winker, D. M., J. Pelon and M. P. McCormick, The CALIPSO mission: Spaceborne lidar for observation of aerosols and clouds, *SPIE Asia-Pacific Symposium on Remote Sensing of the Atmosphere, Environment and Space*, Hangzhou, China, 23-27 October, 4893-01, 2002.

Table 1. Summary of zenith angles and optical depths.

$\theta_0, \theta$	0.0, 18.19, 25.84, 31.78, 36.87, 41.41, 45.57, 49.4653.13, 56.63, 60.0, 63.27, 66.42, 69.51, 72.54, 75.52, 78.46, 81.37, 84.26, 87.13, 90.0
$\psi$	0.0, 2.5, 5.0, 10, 15, 25, 35, 45, 55, 65, 75, 85, 95, 105, 115, 125, 135, 145, 155, 165, 175, 180
$\tau_l$	0.0, 0.25, 0.5, 1, 2, 3, 4, 8, 16, 32, 64, 128
$\tau_w$	0.0, 0.10, 0.20, 0.30, 0.40, 0.50, 0.60, 0.70, 0.80, 0.90, 1.00, 1.20, 1.40, 1.60, 1.80, 2.00, 2.50, 3.00, 3.50, 4.00, 5.00, 7.50, 10.0, 15.0, 20.0, 25.0, 30.0

Table 2. Seasonal mean ice cloud properties for overcast ice cloud TMI FOV's over water, 30°S - 30°N, 1998.

Parameter	JF	MAM	JJA	8-mo. Mean
OCLD MCRS, De ( $\mu\text{m}$ )	61.2	61.5	62.2	61.6
ICLD VISST, De ( $\mu\text{m}$ )	58.1	59.0	58.6	58.6
OCLD VISST, $\tau$	17.5	17.6	19.2	18.1
OCLD MCRS, $\tau$	10.2	10.1	11.3	10.5
ICLD VISST, $\tau$	9.4	9.5	9.6	9.5
OCLD VISST, IWP ( $\text{gm}^{-2}$ )	355	359	393	370
OCLD MCRS, IWP ( $\text{gm}^{-2}$ )	205	206	229	213
ICLD VISST, IWP ( $\text{gm}^{-2}$ )	200	200	201	200

Table 3. Comparison of the mean and standard deviation of  
*IWP* derived from VISST, MCRS and MMCR

	VISST	MCRS	MCRS-SD	MMCR
MEAN	158.8	74.3	59.7	65.1
STDEV	71.5	43.56	44.03	27.3

## Figure Captions

**Figure 1.** Schematic diagram of scattering and absorption processes for the two-layer cloud model.

**Figure 2.** Combined ice and water cloud VIS reflectances at  $\theta_o = 45^\circ$  and  $IWP = 160 \text{ gm}^{-2}$  as functions of  $\theta$  (radial) and  $\psi$  (circular) coordinates.

**Figure 3.** Same as Figure 2, but for fixed  $TWP$ , variable  $IWP$  and  $LWP$ .

**Figure 4.** Variation of diffuse albedo with  $\tau_i$  for CS ice model ( $De = 41 \text{ }\mu\text{m}$ ) for range of lower-layer water cloud optical depths.

**Figure 5.** Variation of TOA diffuse albedo with ice cloud optical depth for different ice models and lower-layer water cloud having  $\tau_w = 2$  and  $r_e = 12 \text{ }\mu\text{m}$ .

**Figure 6.** Variation of TOA diffuse albedo with  $\tau_i$  for different  $r_e$  at  $\tau_w = 30$  and  $De = 30.36 \text{ }\mu\text{m}$ .

**Figure 7.** Variation of TMI  $T_w$  with VIRS  $T_c$  over tropical oceans for (a) ICLD, (b) OCLD, July 1998.

**Figure 8.** Overlapped cloud frequency of occurrence over water surfaces ( $37^\circ\text{S}$ -  $37^\circ\text{N}$ ) during July 1998 as functions of (a) TMI  $LWP_T$  and (b) SST.

**Figure 9.** Seasonal variation of occurrence frequencies for IOWW (solid line), IOSW (dotted line) IOEW (long dashed line) from January to August 1998.

**Figure 10.** Mean effective ice crystal diameter for (a) VISST single-layer and (b) MCRS overlapped overcast ice cloud TMI pixels over water between 30°S and 30°N, June-August 1998.

**Figure 11.** Cloud optical depths from VIRS, June-August, 1998. (a) All ice clouds from VISST analysis. (b) Ice clouds from VISST analysis identified as overlapped (OCLD) by MVI. (c) Ice clouds identified as single-layered (ICLD) by MVI. (d) Same as (b), except from MCRS analysis.

**Figure 12.** Cloud IWP from VIRS, January-February, 1998. (a) All ice clouds from VISST analysis. (b) Ice clouds from VISST analysis identified as overlapped (OCLD) by MVI. (c) Ice clouds identified as single-layered (ICLD) by MVI. (d) Same as (b), except from MCRS analysis. (e) Difference between OCLD analyzed with VISST (b) and MCRS (d).

**Figure 13.** Same as Figure 12, except for June-August 1998.

**Figure 14.** Comparison of IWP derived from MCRS with VISST, and Millimeter Wave Cloud Radar (MMCR) reflectivity for ten cases over ARM Southern Great Plains Central Facility.

**Figure 15.** Variation of optical depth derived from VISST and MCRS as a function of  $LWP_T$  for overcast ice-over-water cloud TMI pixels over ocean (37°S-37°N) during July 1998.

**Figure 16.** Same as Figure 15, except as a function of  $T_w$ .

**Figure 17.** Same as Figure 15, except as function of solar zenith angle.

**Figure 18.** Mean IWP derived from VISST, MVI and MCRS as a function of  $LWP_T$  for overcast ice-over-water cloud TMI pixels over water surfaces (37°S-37°N) during July 1998.

**Figure 19.** Histograms of IWP derived from VISST, MVI and MCRS as functions of  $LWP_T$  for overcast ice-over-water cloud TMI pixels over ocean between 37°S and 37°N during July 1998.





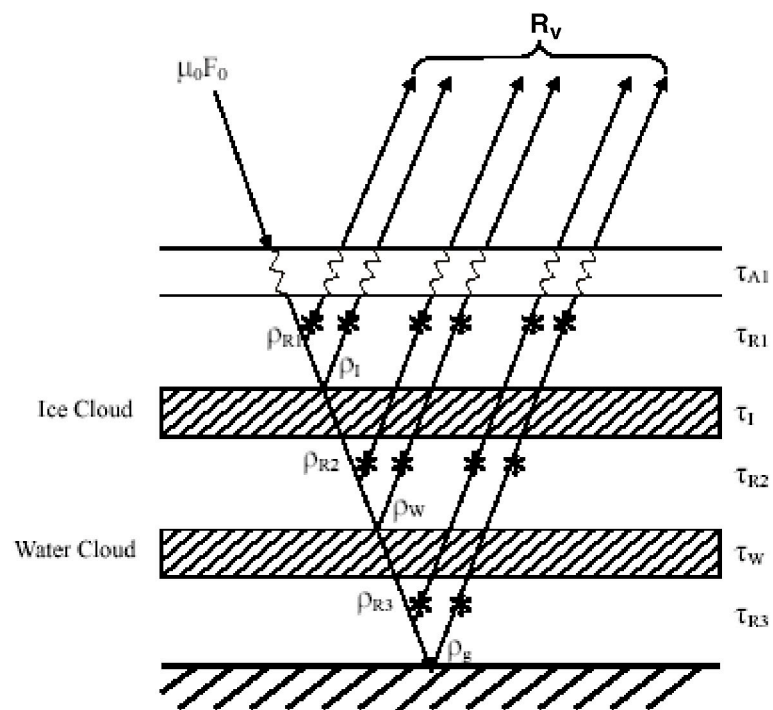


**Figure 1.** Schematic diagram of scattering and absorption processes for the two-layer cloud model.

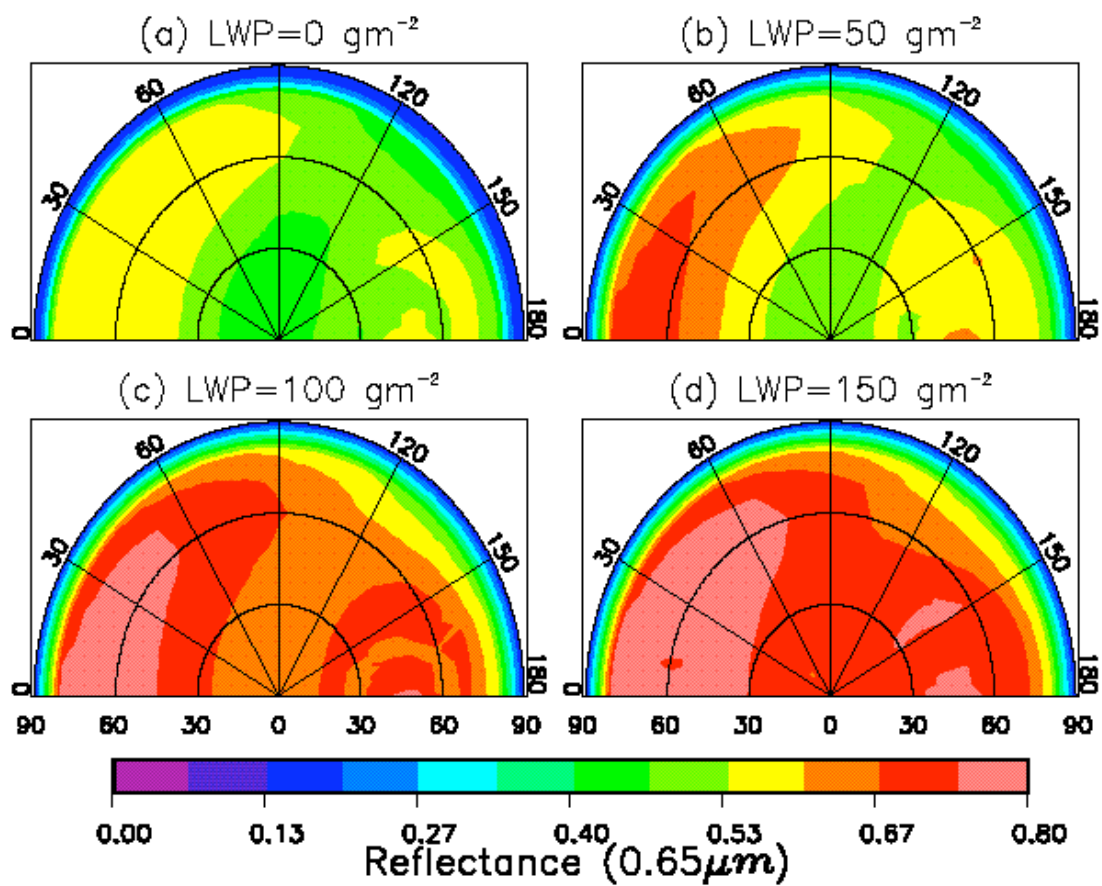


**Figure 2.** Combined ice and water cloud VIS reflectance at  $\theta_o = 45^\circ$  and  $IWP = 160 \text{ gm}^{-2}$  as functions of  $\theta$  (radial) and  $\psi$  (circular) coordinates.

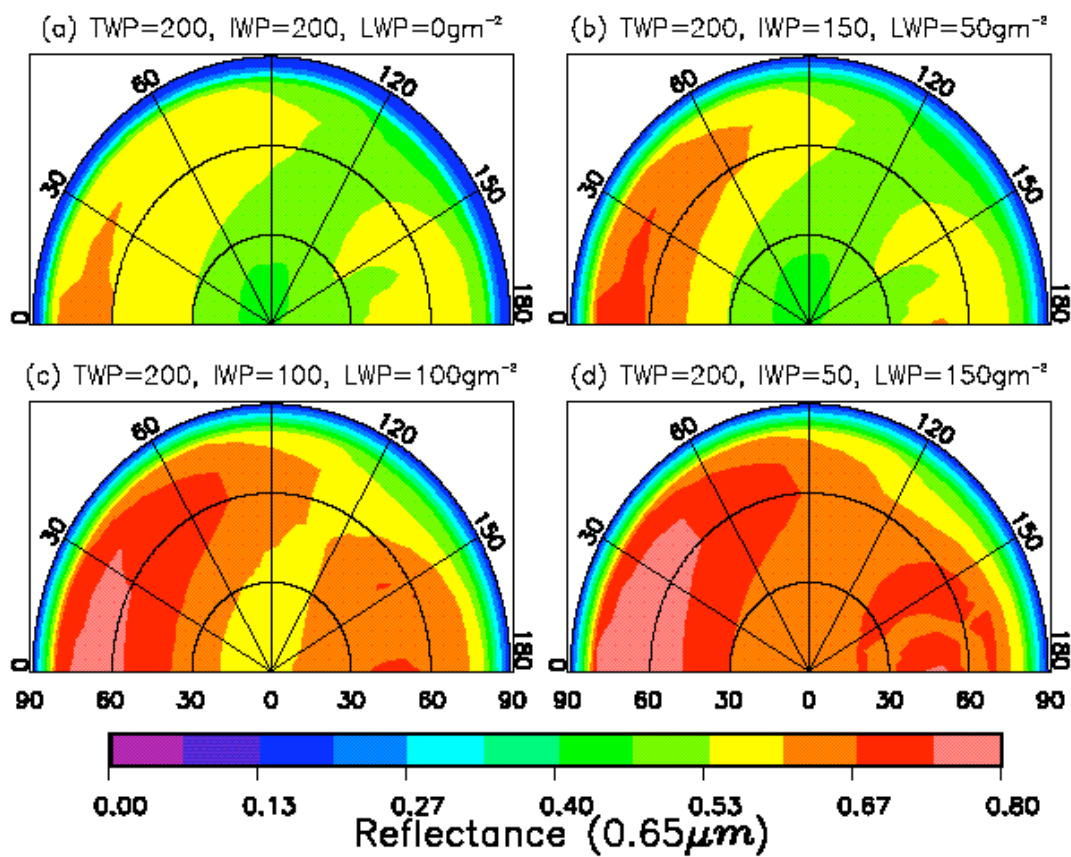


**Figure 3.** Same as Figure 2, but for fixed  $TWP$ , variable  $IWP$  and  $LWP$ .

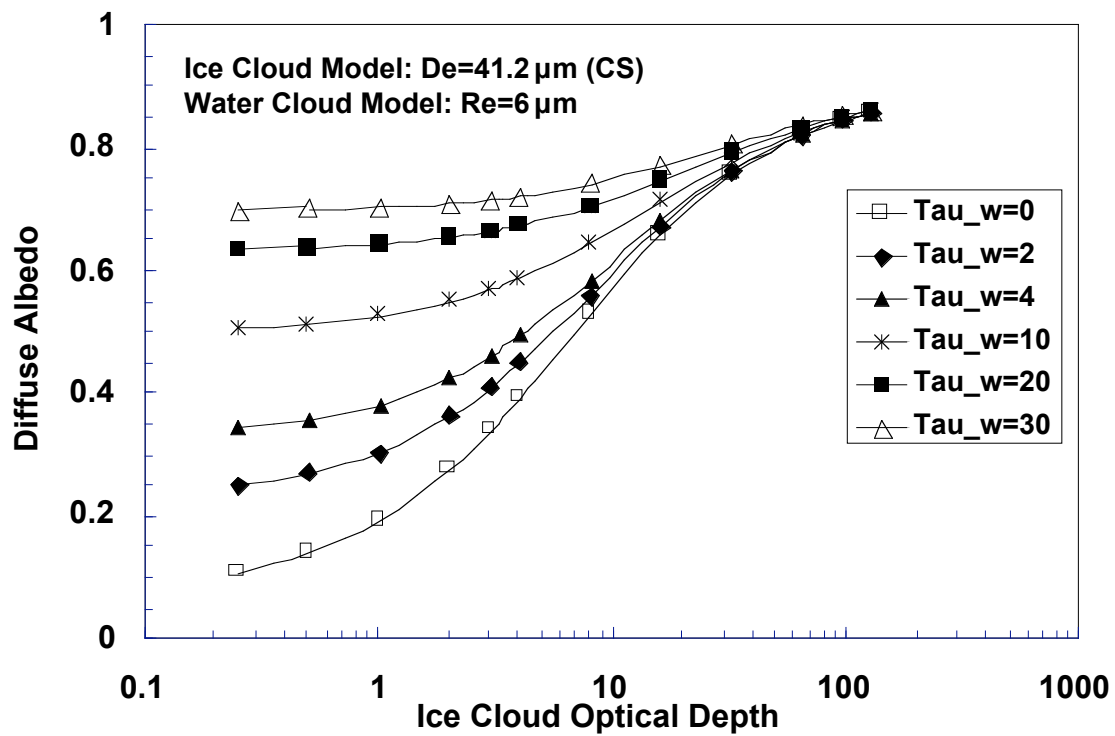


**Figure 4.** Variation of diffuse albedo with  $\tau_i$  for CS ice model ( $De = 41 \mu\text{m}$ ) for range of lower-layer water cloud optical depths.

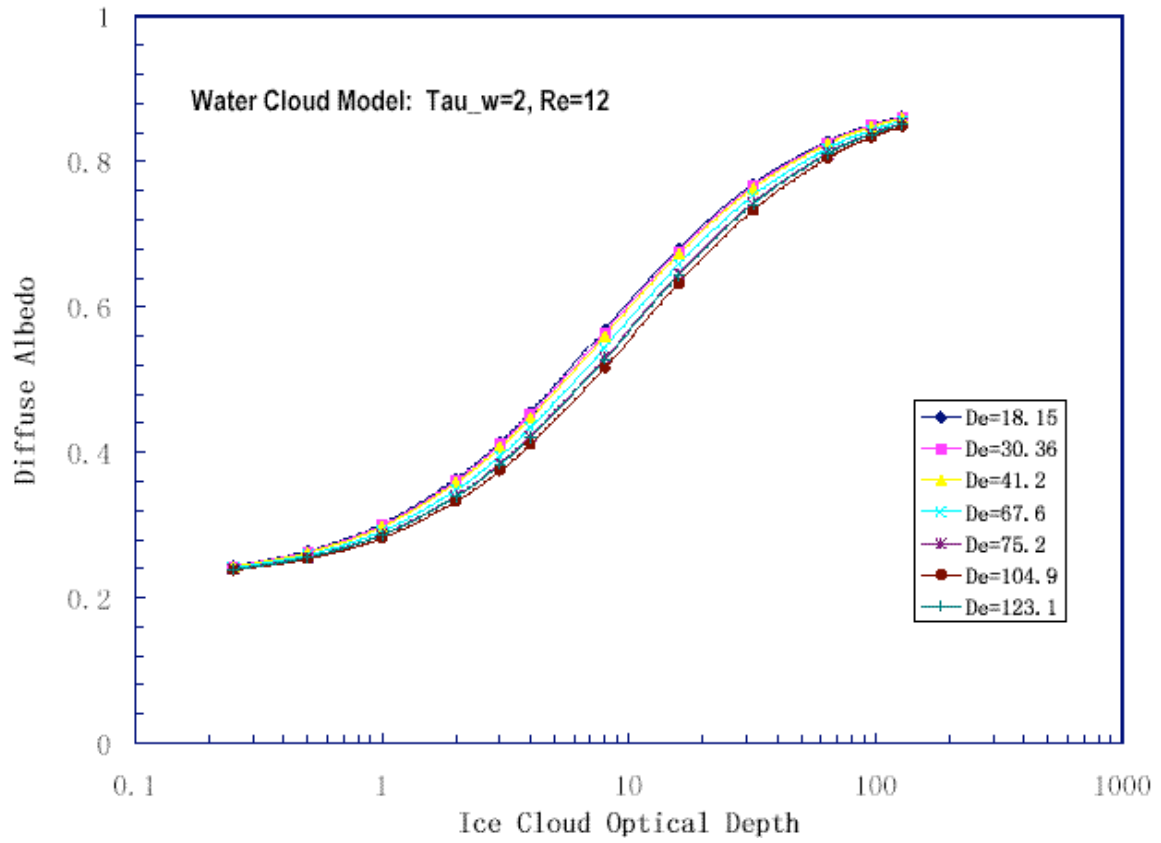


**Figure 5.** Variation of TOA diffuse albedo with ice cloud optical depth for different ice models and lower-layer water cloud having  $\tau_w = 2$  and  $r_e = 12 \mu\text{m}$ .

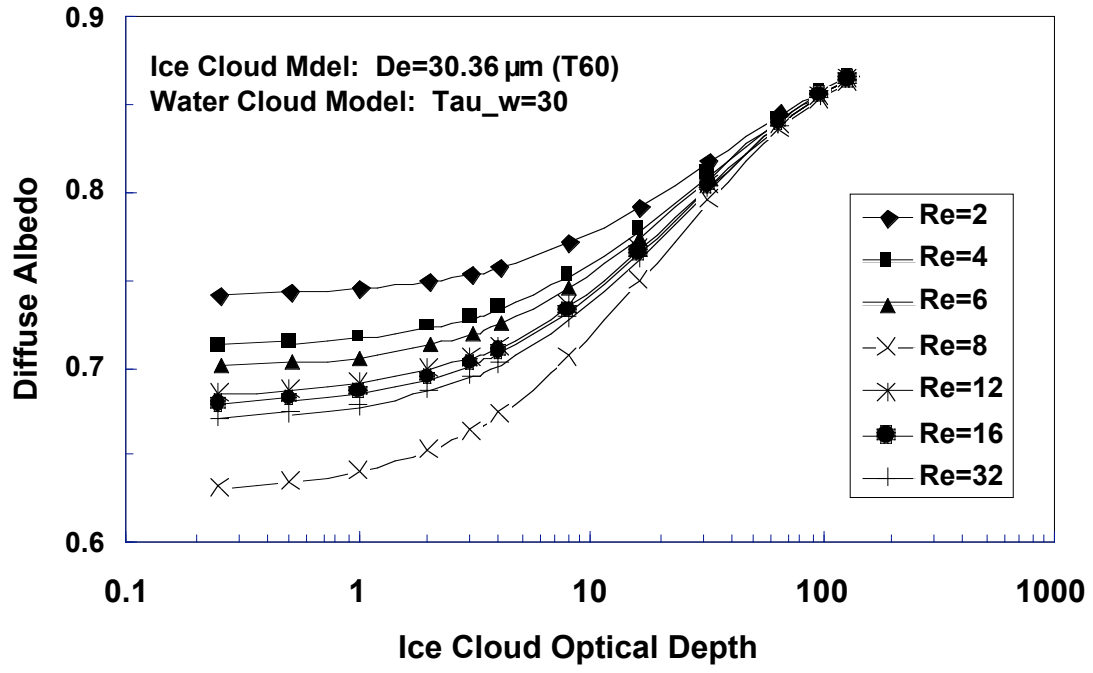


**Figure 6.** Variation of TOA diffuse albedo with  $\tau_l$  for different  $r_e$  at  $\tau_w = 30$  and  $D_e=30.36 \mu\text{m}$ .

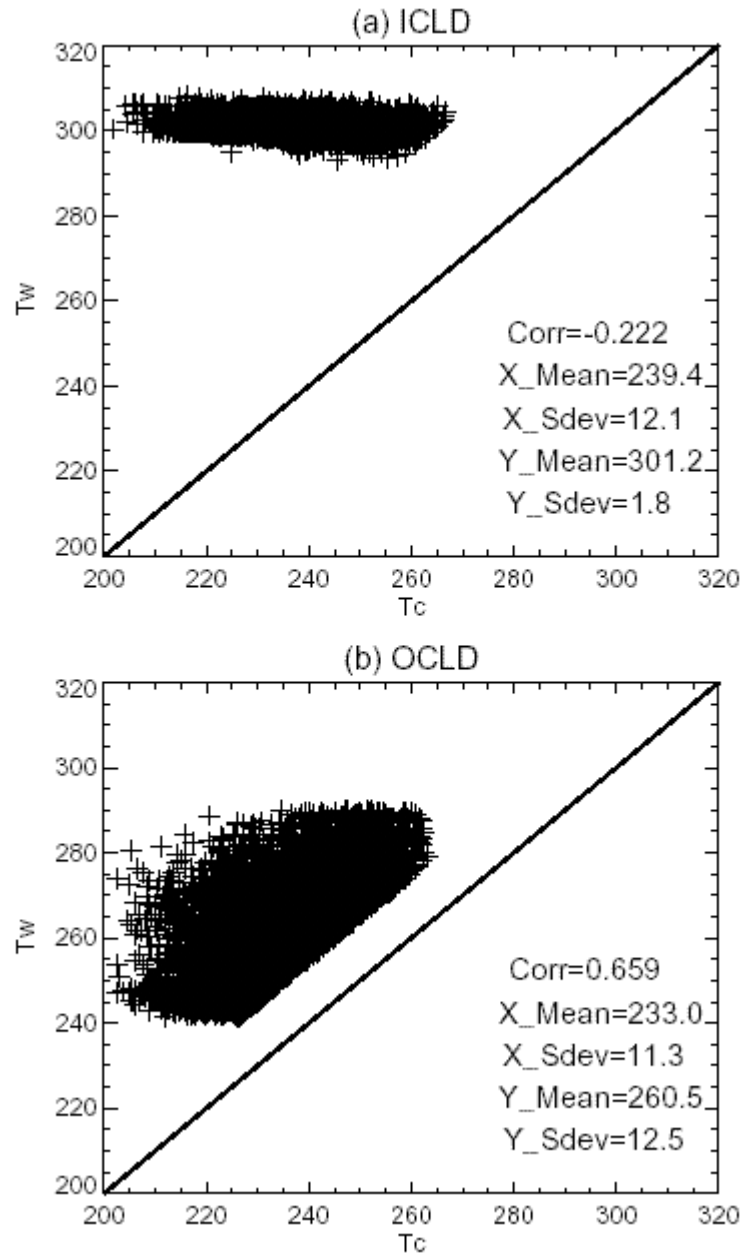


**Figure 7.** Variation of TMI  $T_w$  with VIRS  $T_c$  over tropical oceans for (a) ICLD, (b) OCLD, July 1998.

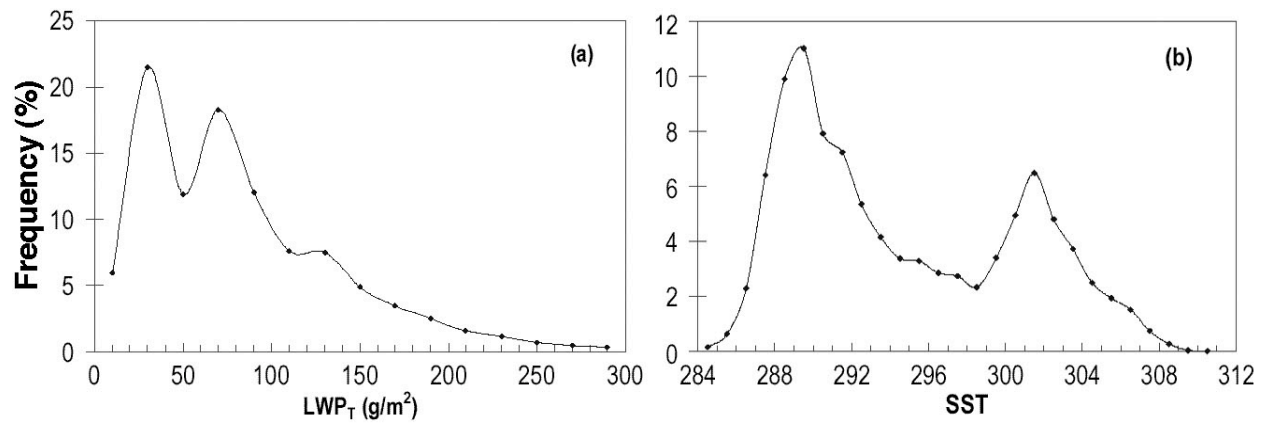


**Figure 8.** Overlapped cloud frequency of occurrence over water surfaces (37°S- 37°N) during July 1998 as functions of (a) TMI LWP<sub>T</sub> and (b) SST;.



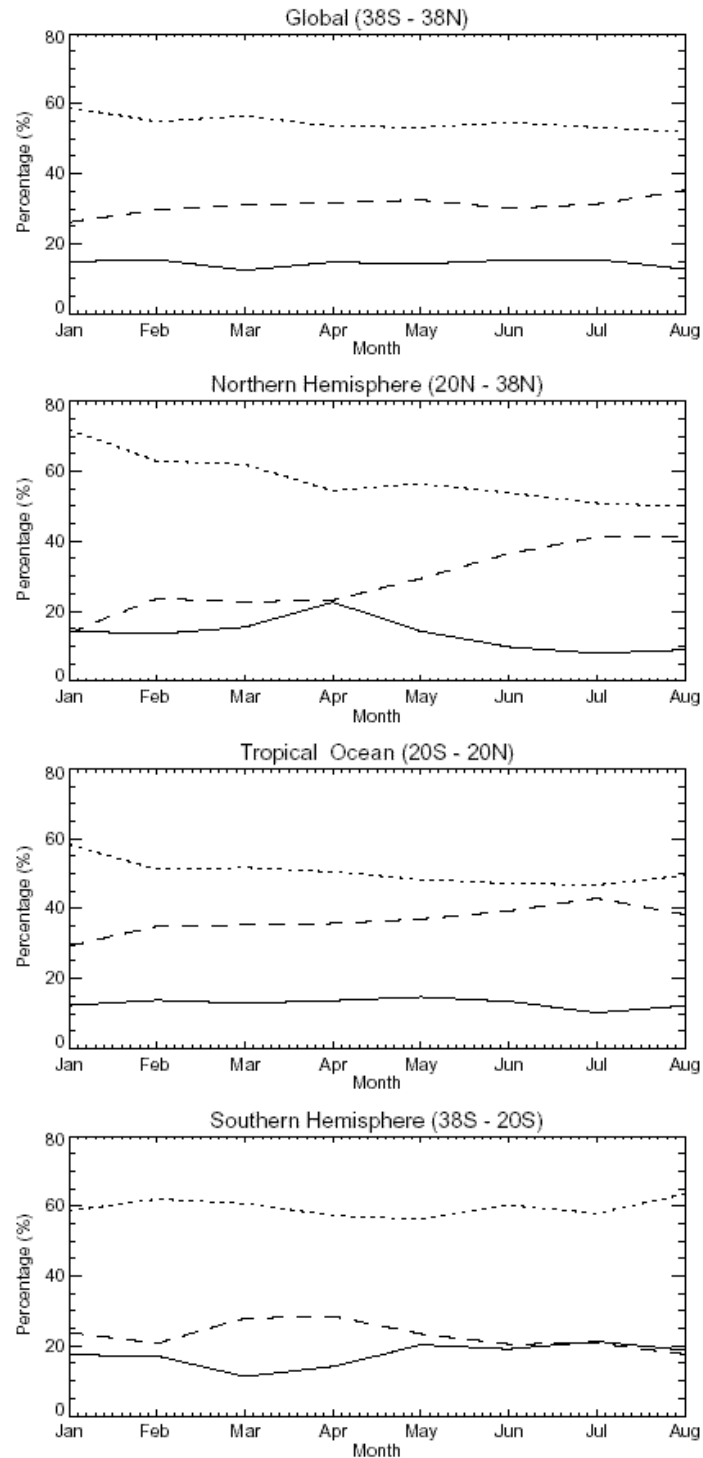


**Figure 9.** Seasonal variation of occurrence frequencies for IOWW (solid), IOSW (dotted), and IOEW (dashed) from January to August 1998.

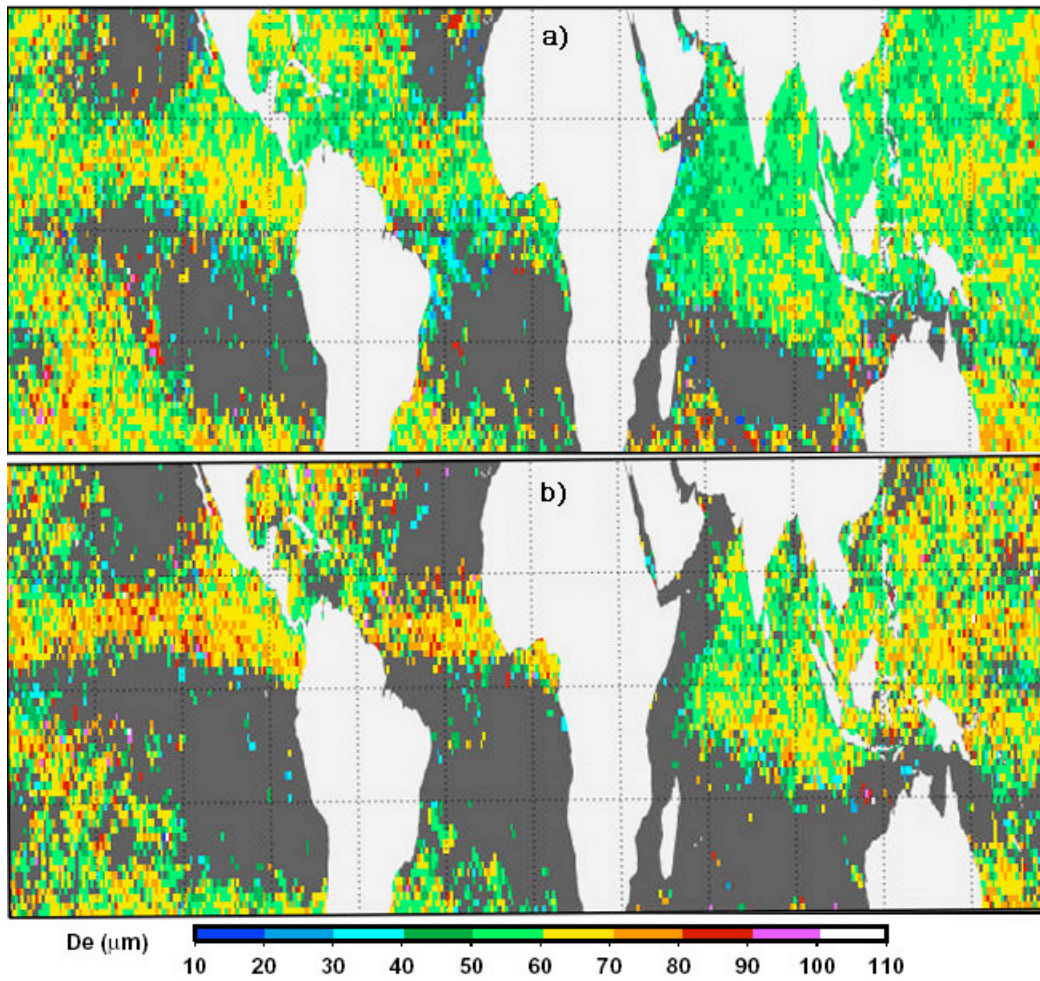


**Figure 10.** Mean effective ice crystal diameter for (a) VISST single-layer and (b) MCRS overlapped overcast ice cloud TMI pixels over water between 30°S and 30°N, June -August 1998.

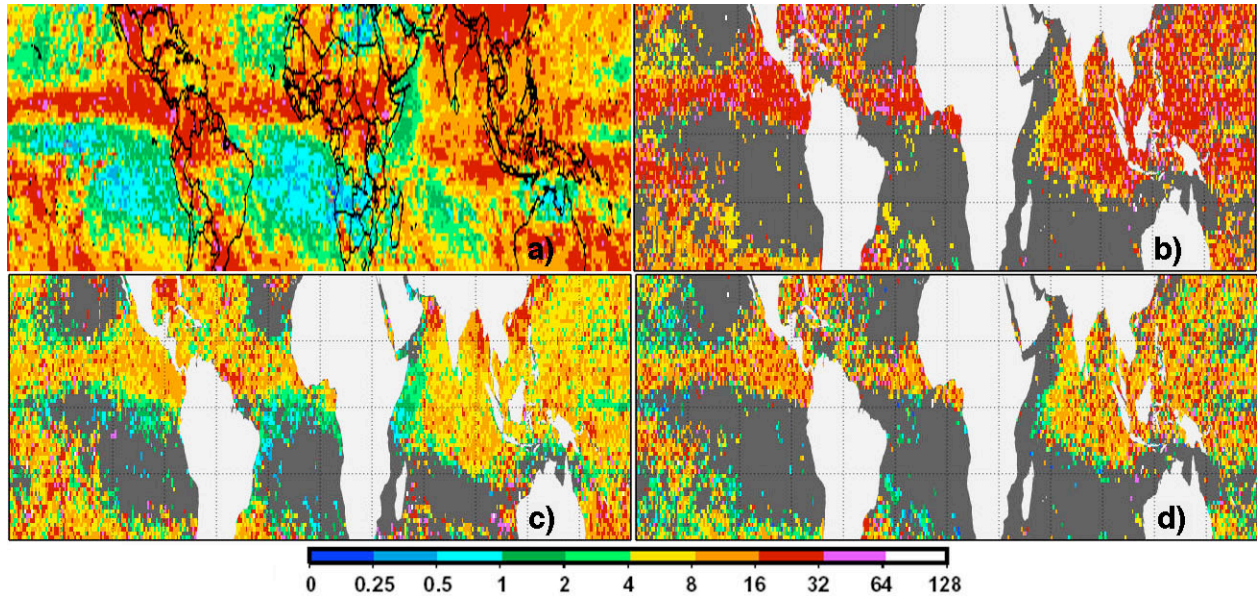


**Figure 11.** Cloud optical depths from VIRS, June-August, 1998. (a) All ice clouds from VISST analysis. (b) Ice clouds from VISST analysis identified as overlapped (OCLD) by MVI. (c) Ice clouds identified as single-layered (ICLD) by MVI. (d) Same as (b), except from MCRS analysis.



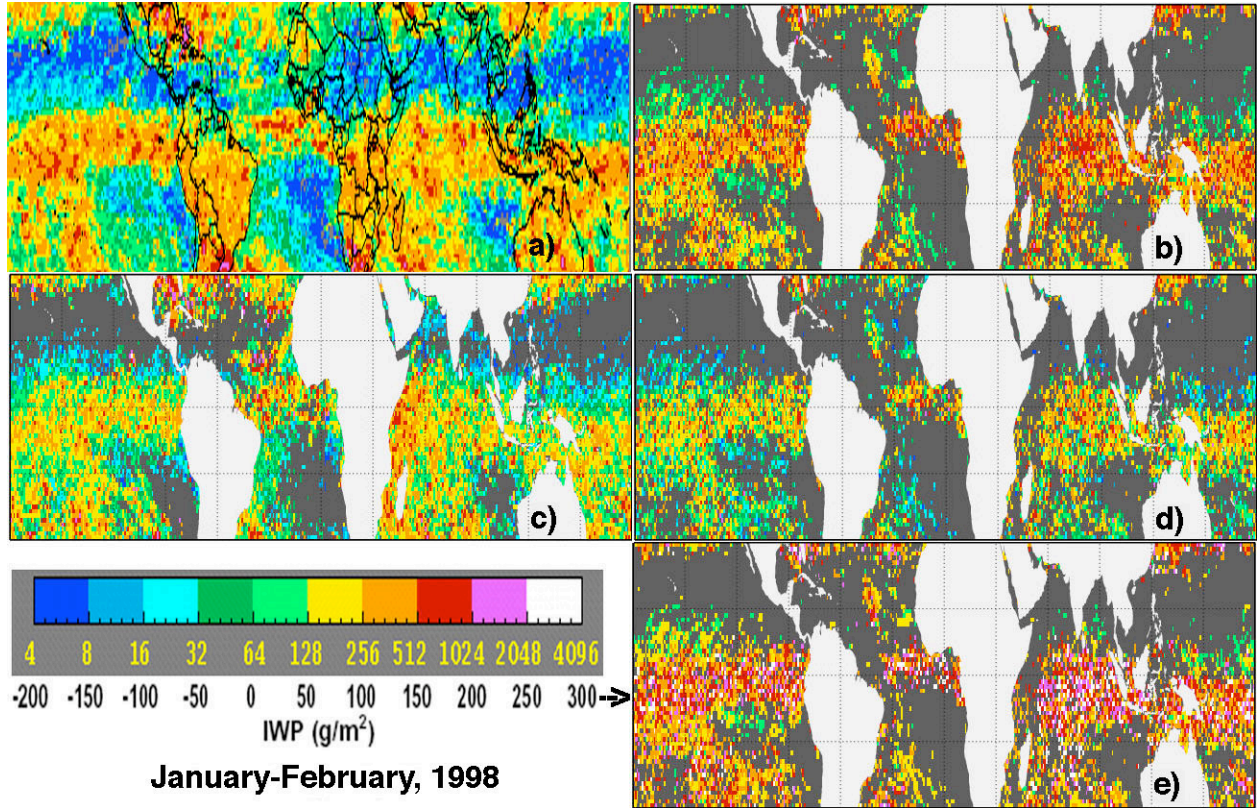


**Figure 12.** Cloud IWP from VIRS, January-February, 1998. (a) All ice clouds from VISST analysis. (b) Ice clouds from VISST analysis identified as overlapped (OCLD) by MVI. (c) Ice clouds identified as single-layered (ICLD) by MVI. (d) Same as (b), except from MCRS analysis. (e) Difference between OCLD analyzed with VISST (b) and MCRS (d).

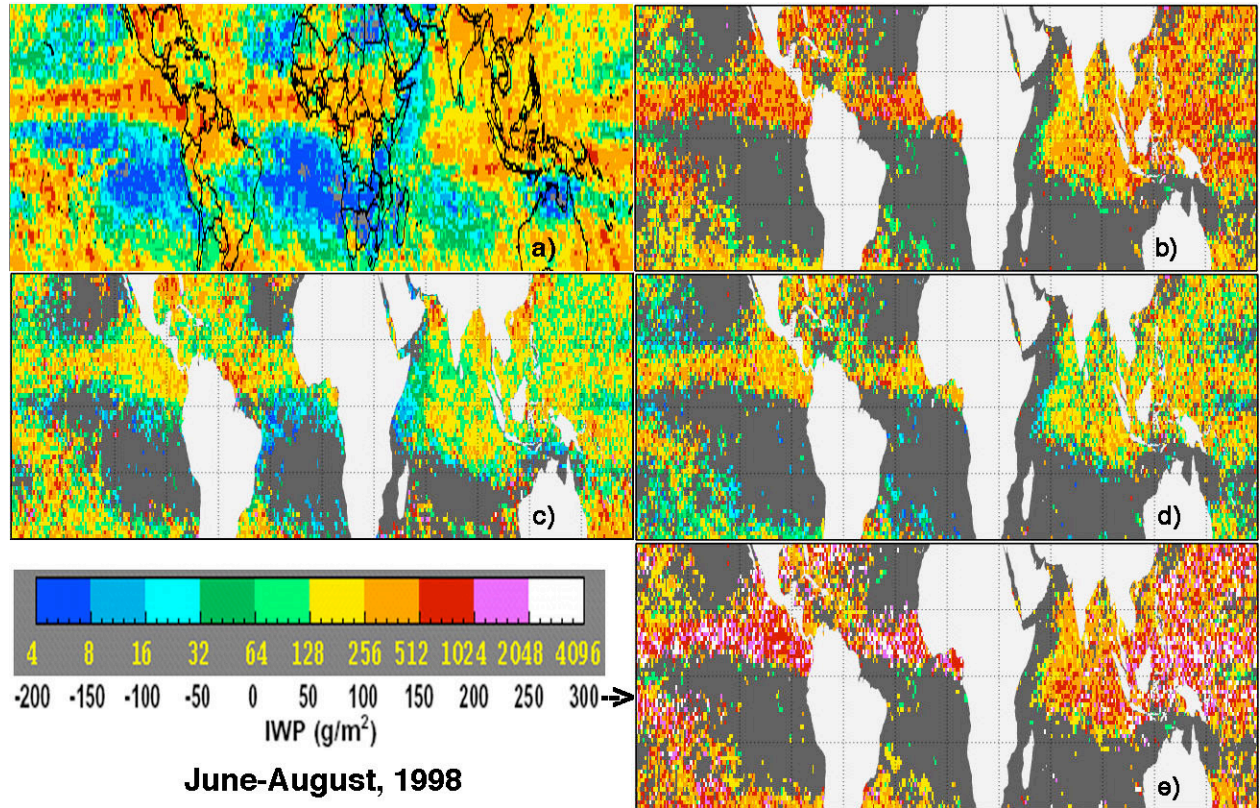


**Figure 13.** Same as Figure 12, except for June-August 1998.

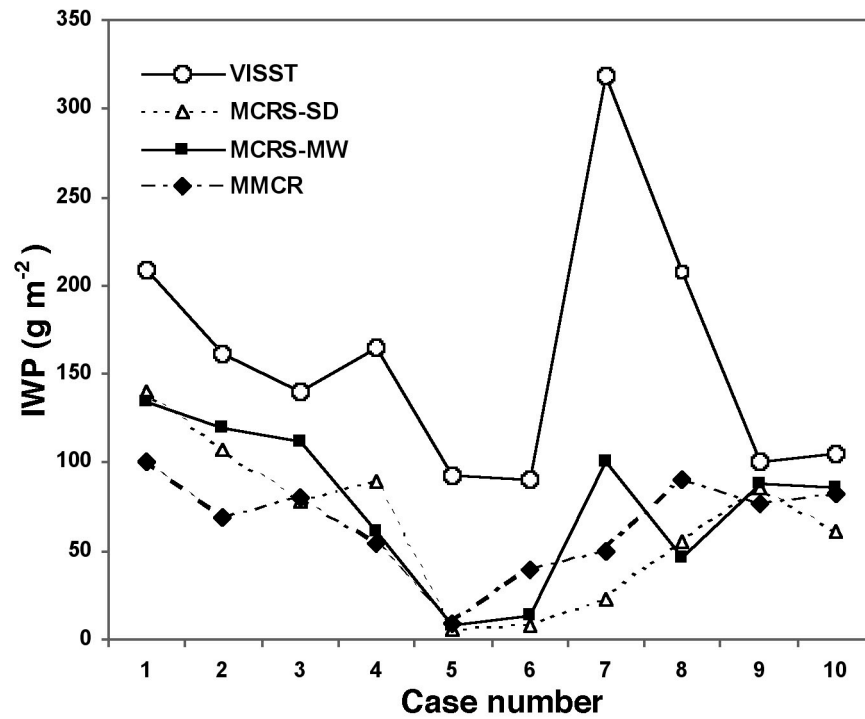


**Figure 14.** Comparison of IWP derived from MCRS with VISST, and Millimeter Wave Cloud Radar (MMCR) reflectivity for ten cases over ARM Southern Great Plains Central Facility.

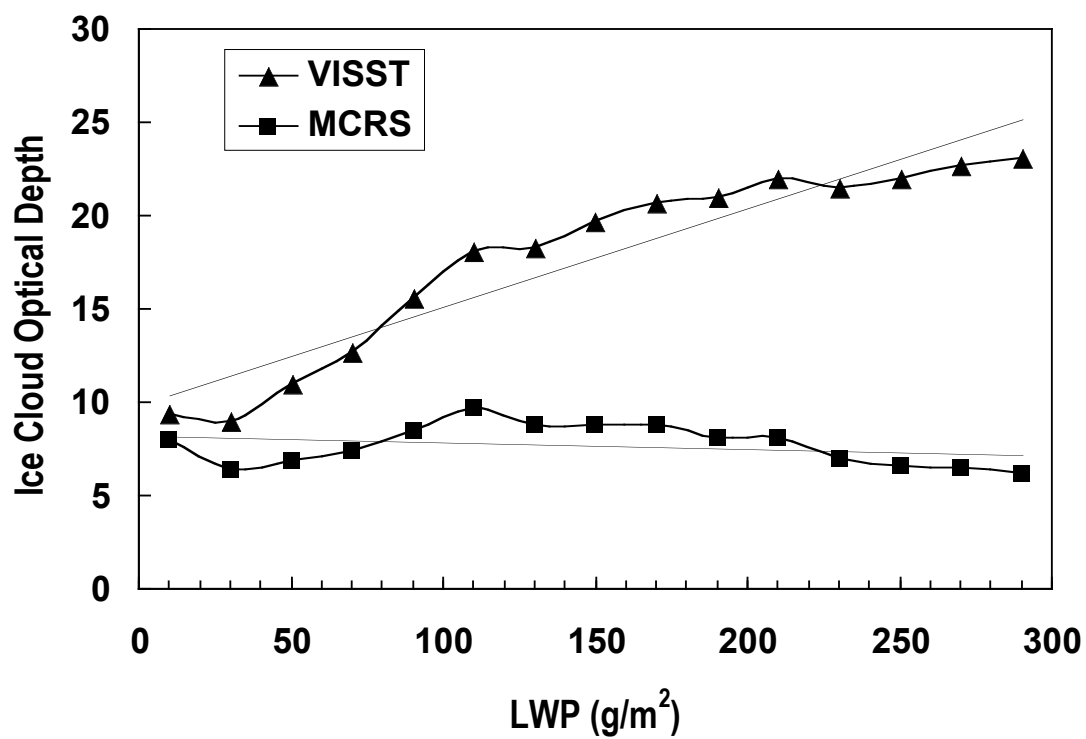


**Figure 15.** Variation of optical depth derived from VISST and MCRS as a function of  $LWP_T$  for overcast ice-over-water cloud TMI pixels over ocean ( $37^\circ\text{S}$ - $37^\circ\text{N}$ ) during July 1998.

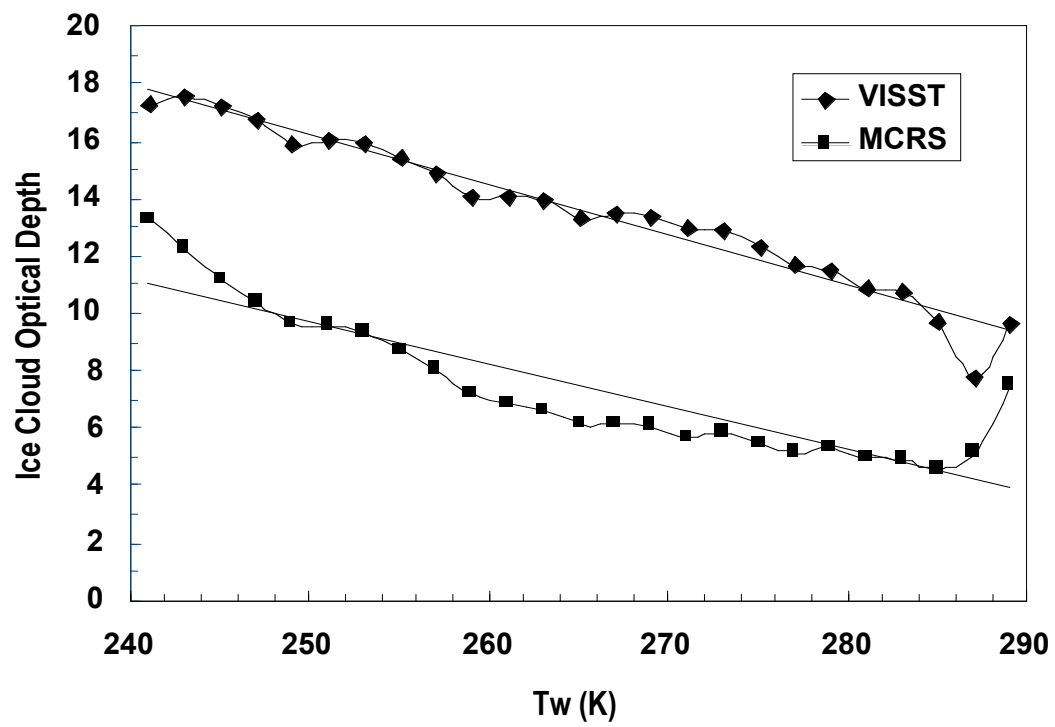


**Figure 16.** Same as Figure 15, except as a function of  $T_w$ .



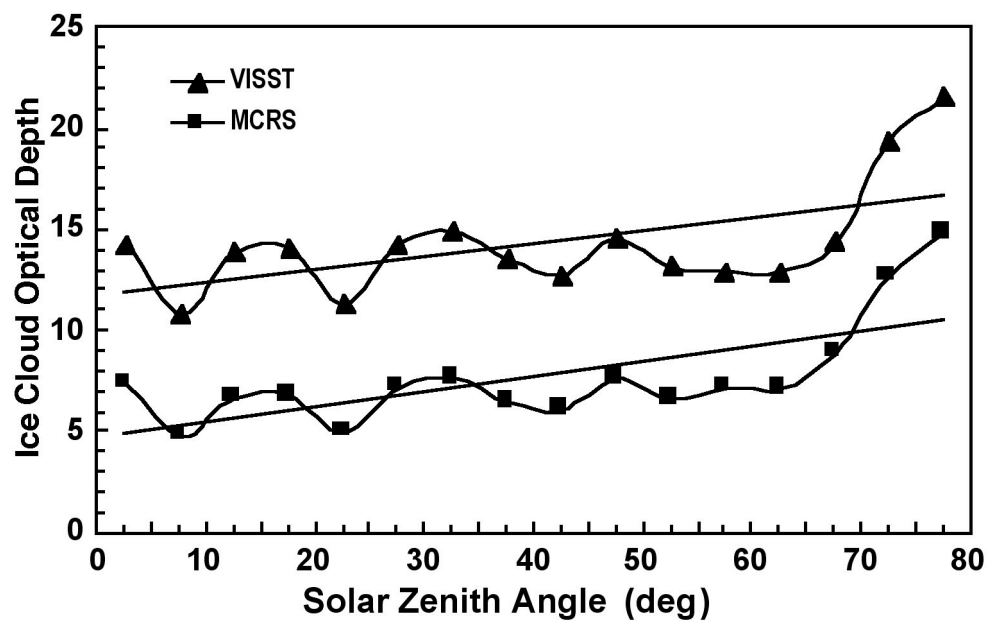


**Figure 17.** Same as Figure 15, except as function of solar zenith angle.

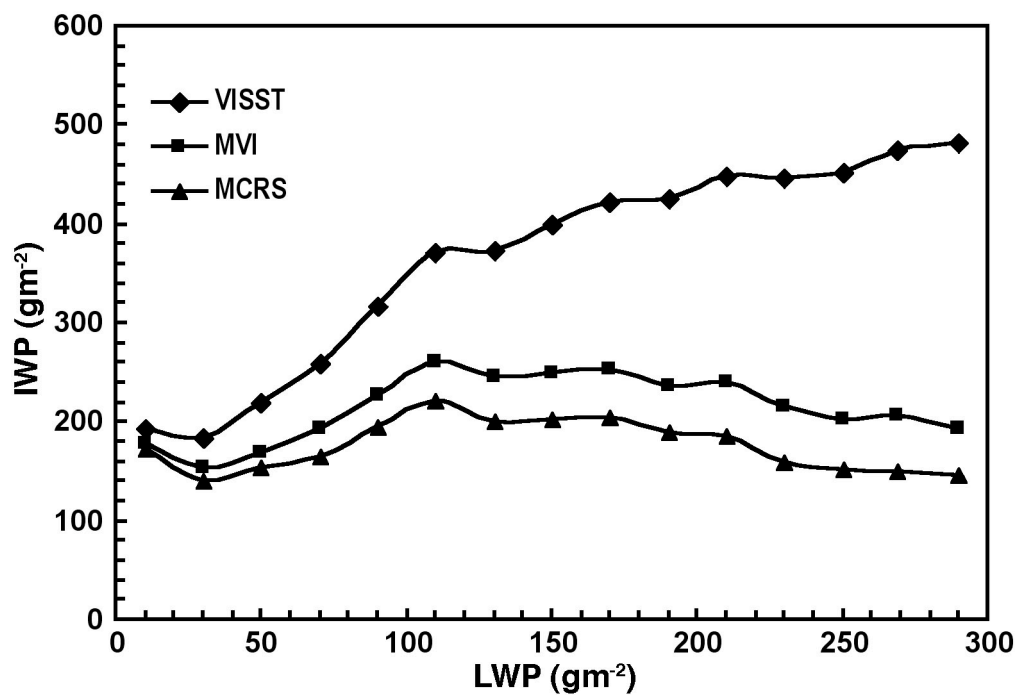


**Figure 18.** Mean IWP derived from VISST, MVI and MCRS as a function of  $LWP_T$  for overcast ice-over-water cloud TMI pixels over water surfaces (37°S-37°N) during July 1998.

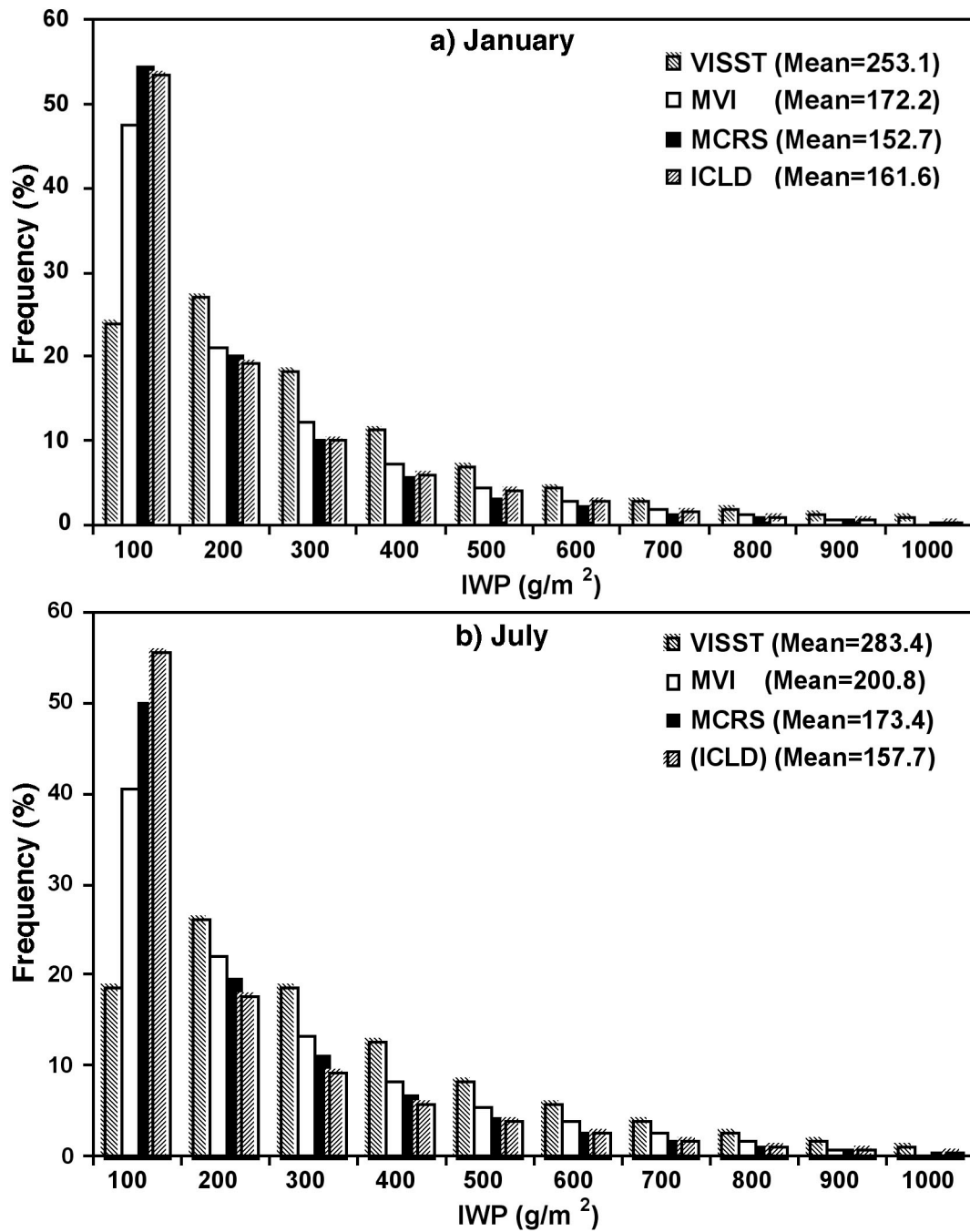


**Figure 19.** Histograms of IWP derived from VISST, MVI and MCRS as functions of  $LWP_T$  for overcast ice-over-water cloud TMI pixels over ocean between 37°S and 37°N during July 1998.